

# Quantifying CO<sub>2</sub> capillary heterogeneity trapping through macroscopic percolation simulation

Hailun Ni<sup>a,b,\*</sup>, Olav Møyner<sup>c</sup>, Kuncho D. Kurtev<sup>d</sup>, Sally M. Benson<sup>a</sup>

<sup>a</sup> Department of Energy Resources Engineering, Stanford University, Stanford, USA

<sup>b</sup> Now at Bureau of Economic Geology, Jackson School of Geosciences, The University of Texas at Austin, Austin, USA

<sup>c</sup> SINTEF Digital, Oslo, Norway

<sup>d</sup> Peter Cook Centre for CCS Research, Department of Infrastructure Engineering, The University of Melbourne, Melbourne, Australia



## ARTICLE INFO

### Keywords:

Macroscopic percolation  
Reduced physics simulation  
CO<sub>2</sub> sequestration  
Multiphase flow  
Residual trapping  
Capillary heterogeneity trapping

## ABSTRACT

Capillary heterogeneity trapping caused by mesoscale heterogeneity at the millimeter scale has been shown to have a great potential in immobilizing a significant amount of CO<sub>2</sub> in CO<sub>2</sub> geologic storage. The goal of this study is to develop and apply a macroscopic percolation simulator to better understand how post-imbibition CO<sub>2</sub> capillary heterogeneity trapping varies with different types and degrees of mesoscale heterogeneity as well as to quantify and compare its contribution to the pore-scale snap-off/bypass residual trapping mechanism. Using invasion percolation during drainage and ordinary percolation with macroscopic trapping during imbibition, the macroscopic percolation simulator can rapidly simulate both post-drainage and post-imbibition CO<sub>2</sub> saturation fields under capillary-gravity equilibrium, producing results that are validated by a full-physics reservoir simulator with a speedup of 10 to 100 times. The macroscopic percolation simulation results have shown that for domains that are completely uncorrelated or with nonleaky downstream capillary barriers, CO<sub>2</sub> heterogeneity trapping contribution always increases with the degree of heterogeneity of the domain. This is consistent with previous experimental results. However, the relationship between the CO<sub>2</sub> residual trapping ability of a domain also depends on the spatial structure of the heterogeneity and trapping ability does not always increase linearly with the degree of heterogeneity as previously shown. Additionally, when the capillary barrier is leaky, then regardless of the degree of heterogeneity, no extra capillary heterogeneity trapping can be achieved after long-term imbibition. Finally, this study demonstrates how residual trapping relationships may not be scale-invariant and calls for more sophisticated upscaling methods such as the macroscopic percolation simulation method presented here.

## 1. Introduction

CO<sub>2</sub> geologic storage is an integral part of the climate change solutions that allow the society to transition toward carbon neutral energy while still relying on fossil fuels (IPCC, 2014, 2005; Rogelj et al., 2018). There are several secondary trapping mechanisms that provide extra immobilization security of the CO<sub>2</sub> plume in addition to the cap rock primary trapping mechanism. Residual trapping by capillary forces is one such secondary trapping mechanism that is capable of immobilizing a significant amount of CO<sub>2</sub> (IPCC, 2005). Conventionally, the pore-scale snap-off and bypass mechanisms are considered to be the main trapping mechanisms responsible for residual trapping (Krevor et al., 2015). However, recent studies have shown that mesoscale heterogeneity at the millimeter to centimeter scale also plays an important role in residually trapping the nonwetting phase fluid, causing what is known as capillary heterogeneity trapping (Corbett et al., 1992;

Huang et al., 1995; Jackson and Krevor, 2020; Kortekaas, 1985; Krevor et al., 2011; Meckel et al., 2015; Saadatpoor et al., 2010; Trevisan et al., 2017).

A few simulation studies have previously investigated capillary heterogeneity trapping of CO<sub>2</sub> or other nonwetting phase fluid such as oil under capillary dominated flow regimes. A significant portion of the literature on this topic focuses on capillary heterogeneity trapping due to buoyancy flow (Behzadi et al., 2011; Gershenson et al., 2017; Meckel et al., 2015; Ren et al., 2019; Ren and Duncan, 2019; Saadatpoor et al., 2013, 2010; Trevisan et al., 2017), and just a few examine post-imbibition capillary heterogeneity trapping, the topic of this study (Corbett et al., 1992; Kortekaas, 1985; Ren, 2018). Kortekaas (1985) through mathematical simulation found that when water imbibition direction is perpendicular to the lamination, oil capillary heterogeneity trapping occurs when inter-laminae permeability contrast is present. The same conclusion is reached by

\* Corresponding author at: 10611 Exploration Way, Rm. 2.102Q, Austin, TX 78758, USA.  
E-mail address: [hailun.ni@beg.utexas.edu](mailto:hailun.ni@beg.utexas.edu) (H. Ni).

Corbett et al. (1992) with an ECLIPSE black oil simulator. More recently, Ren (2018) conducted 2D reservoir-scale simulations with the CMG-GEM simulator and reported that the amount of capillary heterogeneity trapping is intrinsic to the heterogeneity of the domain. Later, Ren et al. (2019) used an analytical method to identify and quantify the capillary heterogeneity trapping amount. However, Ren et al.'s method only obtains the upper bound of the capillary heterogeneity trapping capacity and does not consider any contribution from pore-scale residual trapping. Therefore, it is of interest to develop a simulation method that can enable rapid and accurate quantification of both the mesoscale capillary heterogeneity trapping amount and the pore-scale residual trapping amount of any heterogeneous domain in order to measure total post-imbibition residual trapping and the relative importance of the two residual trapping mechanisms.

However, full-physics reservoir simulators, such as the MATLAB Reservoir Simulation Toolbox (MRST) that is used in this study, are not well suited to the task of simulating low rate injection scenarios on domains with a high degree of capillary heterogeneity. Full physics reservoir simulations take a long simulated time to reach capillary equilibrium as many pore volumes of fluid need to be injected into the domain. They can also take a long wall clock time to run when flow rates are low because small time steps are needed to ensure convergence. This itself is because large contrasts in capillary pressure characteristic curves resulting from capillary heterogeneity can lead to convergence problems, particularly at very low flow rates. A type of reduced physics simulator based on macroscopic percolation (MP) can overcome such challenges (Ioannidis et al., 1996; Kueper and McWhorter, 1992; Yortsos et al., 1993). This type of simulator applies the pore-scale microscopic percolation displacement algorithms to macroscopic voxels with well-defined continuum-scale properties such as porosity, permeability, and saturation, hence the term “macroscopic”. The MP simulator is best applied when capillary forces dominate the flow regime and there is no significant viscous impact on flow. One major advantage of an MP simulator is that it can easily handle highly discontinuous and heterogeneous domains because the highly nonlinear dynamic multiphase flow displacement processes are not modeled. Another advantage of an MP simulator is the significant amount of speedup in simulation time that is achievable (Celia et al., 2015).

In the CO<sub>2</sub> storage field, Permedia's CO<sub>2</sub> Migration module is a widely-used industry MP simulator (Cavanagh and Haszeldine, 2014; Meckel et al., 2015; Trevisan et al., 2017). Cavanagh and Haszeldine (2014) first applied Permedia to history-match CO<sub>2</sub> plume migration at the Sleipner site. Meckel et al. (2015) and Trevisan et al. (2017) have also utilized this tool to investigate how the amount of domain average post-drainage CO<sub>2</sub> saturation varies with different types and degrees of heterogeneity. However, Permedia's original purpose is to model hydrocarbon migration. As a consequence, Permedia assigns only one of two saturation values to all invaded voxels. They are the irreducible water saturation for the voxels accumulating CO<sub>2</sub> behind a capillary barrier, and the breakthrough CO<sub>2</sub> saturation for the voxels on the migration path. This simple formulation does not allow Permedia to report the more heterogeneous saturation fields often seen in coreflooding experiments. Furthermore, Permedia can only simulate nonwetting phase drainage and not wetting phase imbibition.

A number of past studies have presented MP formulations for generating domain effective relative permeability and capillary pressure curves for heterogeneous domains for both drainage (Jackson and Krevor, 2020; Yang et al., 2013) and imbibition (Nooruddin and Blunt, 2018; Wolff et al., 2013; Yang et al., 2020). Therefore, the MP algorithm can be used to generate upscaled properties to be used as inputs into full-physics simulators to simulate CO<sub>2</sub> plume migration in order to save computational resources and increase simulation speeds, as is done by Jackson and Krevor (2020). Yet, the MP simulator can also be directly applied to field-scale domains due to the simplicity of the MP algorithm and its small computational burden. In this study, we will present just one such field-scale MP simulation example.

By developing a fast and reliable MP simulator, the current study aims to answer the following two questions for heterogeneous domains: How does residual trapping ability vary with different types and degrees of mesoscale heterogeneity? And does the residual trapping relationship remain unchanged across scales? The rest of this study is organized as such. First the MP simulation model, model inputs, and input data will be presented. Then the MP simulation results will be discussed. Two kinds of simulation cases are presented that 1) predict residual trapping abilities on different types of permeability fields, and 2) demonstrate how the MP simulator can be applied to a field-scale domain.

## 2. The MP simulation model

The MP simulation model is a reduced physics simulator that rapidly estimates the distribution of CO<sub>2</sub>/water saturations under strongly capillary dominated flow regimes. By applying two-phase flow and trapping rules, the MP simulator can estimate CO<sub>2</sub> residual trapping during post-injection imbibition. The core idea of the MP simulation model is to reduce computation complexity by simulating quasi-static equilibrium states (Ioannidis et al., 1996). It involves increasing or decreasing an externally imposed capillary pressure on the domain in discrete steps in order to simulate nonwetting phase saturation during drainage and wetting phase imbibition after drainage. At each such capillary pressure step, the saturation field can be computed from the set of input capillary pressure curves for each voxel.

At the voxel level, the only necessary input into the MP simulator is the drainage and imbibition capillary pressure curves that govern the voxel saturation at a specified capillary pressure. While it is relatively straightforward to simulate the drainage process, one major challenge in building the MP simulation model is to equip it with the ability to accurately capture both pore-scale and mesoscale residual trapping during the imbibition process. In conventional reservoir simulation, pore-scale residual trapping is modeled by adding hysteresis to the voxel-level imbibition capillary pressure curves. In conventional MP simulation, mesoscale residual trapping, or capillary heterogeneity trapping, is modeled by adding macroscopic trapping rules during imbibition. However, to simulate residual trapping for both scales at the same time is not as simple as directly combining voxel-level hysteresis with macroscopic trapping rules.

Previously, Nooruddin and Blunt (2018) applied the aforementioned simple combination method and reported that essentially no post-imbibition nonwetting phase capillary heterogeneity trapping is present in their MP simulations for water-wet rocks. This is because the authors followed the conventional approach by allowing the voxel-level capillary pressure to reduce to 0 at the residual saturation during imbibition simulation. However, when this is the case, it has been confirmed that no extra capillary heterogeneity trapping can be achieved in either MP simulations or full-physics simulations with enough pore volumes injected (PVI) (Bech and Frykman, 2018; Ioannidis et al., 1996; Jackson and Krevor, 2019; Kueper and McWhorter, 1992). These simulation results run contrary to the fact that a significant amount of post-imbibition capillary heterogeneity trapping has been observed in water-wet sandstone coreflooding experiments (Krevor et al., 2011). Therefore, key modifications to both the voxel-level hysteresis model and the macroscopic trapping rules are needed to better match reality.

These modifications include setting the imbibition snap-off pressure  $P_s$  to be nonzero (Jackson et al., 2020; Jackson and Krevor, 2019) and applying an additional domain-level macroscopic trapping rule when the  $P_s$  value is reached during the MP imbibition simulation. We assume that this nonzero continuum-scale snap-off capillary pressure  $P_s$  occurs at the residual saturation caused purely by pore-scale residual trapping mechanisms, and that this is the capillary pressure below which the nonwetting phase is no longer continuous during imbibition. With these assumptions in place, the voxel-level hysteretic capillary pressure model should then terminate at its  $P_s$  value during imbibition and does not further decrease. For the MP imbibition simulation process, this means

it is necessary to implement a macroscopic trapping rule that freezes the domain saturation during imbibition when the externally imposed capillary pressure drops below this specified  $P_s$  value to ensure that the nonwetting phase is no longer flowing. While some studies have adopted lower  $P_s$  values (Jackson et al., 2020; Jackson and Krevor, 2019), in this study, we set the  $P_s$  value equal to the voxel-level capillary entry pressure  $P_e$  value for simplicity. Although determining the exact value for  $P_s$  is outside the scope of the current study,  $P_s$  does directly affect the MP residual trapping simulation results. Therefore, a sensitivity analysis has been conducted on the value of  $P_s$  and is provided in Appendix A.

Because the MP simulator is a reduced physics simulator, several assumptions are employed in the current study. The flow rate is assumed to be infinitesimal, such that viscous forces are negligible. It is also assumed that capillary pressure equilibrium is instantly reached at every pressure step. Each voxel in the domain is assumed to be at the continuum scale so that they would have well-defined voxel-level petrophysical and multiphase flow properties, i.e. porosity, permeability, and capillary pressure curves. The MP simulations in this study are run on 3D domains. For boundary conditions, both the inlet and the outlet slices are constant pressure boundaries. All the other boundaries are no-flow boundaries. Drainage simulations start at 100% water saturation everywhere in the domain, and imbibition simulations start with the post-drainage saturation field. In other words, first a primary drainage and then a secondary imbibition are simulated.

To demonstrate that the MP simulator is a suitable tool for simulating realistic CO<sub>2</sub> storage projects at the field scale, a scaling group analysis has been conducted. Field-scale CO<sub>2</sub> storage has a viscosity ratio ( $\mu_w/\mu_{nw}$ ) of  $\sim 10^1$ , where  $\mu_w$  and  $\mu_{nw}$  are viscosity for the wetting and the nonwetting phase. The field-scale microscopic Bond number ( $\Delta\rho g d^2/\sigma$ ) is  $10^{-3}$ , where  $\Delta\rho$  is the density difference between the two phases,  $g$  is the gravity acceleration constant,  $d$  is the mean pore diameter, and  $\sigma$  is the interfacial tension (Cinar et al., 2007; Kimbrel et al., 2015; Morrow et al., 1988). During CO<sub>2</sub> injection when we are away from the well and during the post-injection fluid redistribution stage, the field-scale range of the capillary number ( $v\mu/\sigma$ ) computed is  $10^{-12}$  to  $10^{-8}$ , where  $v$  is the Darcy velocity and  $\mu$  is the viscosity of the invading fluid (Larkin, 2010; Lefebvre du Prey, 1973; Morrow et al., 1988). Finally the gravity number ( $\Delta\rho g k/v\mu$ ) value range at the field scale is  $10^0$  to  $10^3$ , where  $k$  is average permeability (Engelberts and Klinkenberg, 1951; Larkin, 2010). MP simulations have the same viscosity ratio and microscopic Bond number values as the previous field-scale values. Because the flow rate is taken to be zero in MP simulations, the capillary number of any MP simulation is 0 and the gravity number is infinite, which are also consistent with the strongly capillary and gravity dominated flow regime at the field scale. The calculation details can be found in the supplementary material.

The rest of this section describes the details of the MP simulation formulation and the inputs into the simulator. Here, an algorithm-based MP simulator formulation is presented. For a matrix representation of the MP simulator, see Nooruddin and Blunt (2018).

### 2.1. Voxel-level inputs

Voxel-level properties need to be specified as inputs into the MP simulator. Strictly speaking, the MP simulator only requires capillary pressure curves to be defined at the voxel level. The input voxel-level capillary pressure curves can be Brooks-Corey, van Genuchten, or any user-defined models. In this study, we use a Brooks-Corey model for capillary pressure curves, so that a nonzero capillary entry pressure exists. The Leverett J-function scaling relationship has been shown to provide accurate modeling of core-scale experiments. It is a convenient way to assign different capillary pressure curves to voxels and has been widely used as a way to model capillary heterogeneity Huang et al., 1995; Krause et al., 2013, 2011; Kuo and Benson, 2015; Saadatpoor et al., 2010; Zeybek et al., 1995). A single J function can be scaled according to the voxels' porosity and permeability values to generate voxel-

level capillary pressure curves for voxels belonging to a single rock formation (Akin et al., 2000; Leverett, 1941; Li and Benson, 2015). The equations used to represent the drainage voxel-level capillary pressure curves are shown in Eqs. (1) to (4) (Brooks and Corey, 1964; Pini and Benson, 2017),

$$P_{c,j}^D = \alpha \cdot P_e J \quad (1)$$

$$J = S_w^{*-1/\lambda} \quad (2)$$

$$S_w^* = \frac{S_w - S_{wi}}{1 - S_{wi}} \quad (3)$$

$$\alpha = \sqrt{\frac{k_{avg} \phi_j}{\phi_{avg} k_j}} \quad (4)$$

where  $P_{c,j}^D$  is the drainage capillary pressure of each voxel  $j$ ,  $J$  is the J function,  $S_w^*$  is the effective wetting phase (water) saturation, and  $\alpha$  is the scaling factor that converts the average capillary pressure curve to the voxel-level curves. In Eq. (1),  $P_e$  is the domain capillary entry pressure of the Brooks-Corey model. In Eq. (2),  $\lambda$  is the pore size distribution index. In Eq. (3),  $S_w$  is the water saturation and  $S_{wi}$  is the irreducible water saturation. In Eq. (4),  $\phi_{avg}$  and  $k_{avg}$  are the average porosity and permeability values, while  $\phi_j$  and  $k_j$  are the voxel-level porosity and permeability values. Note that for field-scale simulations, different  $\phi_{avg}$  and  $k_{avg}$  values should be specified for every rock type. After the Leverett J-function scaling relationship is applied, when the voxels are at capillary equilibrium, the saturation of the voxels would all be different with respect mainly to their permeability values, as illustrated in Fig. 1.

The case for the imbibition capillary pressure curves is more complex because hysteresis is present. We can choose to simply use the non-hysteretic drainage capillary pressure curves during imbibition. However, this is not realistic when comparing to experimental results. In order to account for hysteresis caused by pore-scale trapping mechanisms, we use a trapping model like the Land or the linear trapping relationship. In this study, the linear trapping relationship is used unless otherwise specified. The equations used to represent the imbibition hysteretic voxel-level capillary pressure curves are shown in Eqs. (5) to (9) (Jackson et al., 2020; Pini and Benson, 2017),

$$P_{c,j}^I = \alpha \cdot \left[ P_{ci} \left( \left( 1 - S_{nw,m}^* \right)^{-1/\lambda} - 1 \right) + P_s \right] \quad (5)$$

$$P_{ci} = \left( P_e - P_s S_{w,i}^* \right)^{-1} \left( 1 - S_{w,i}^* \right)^{-1} \quad (6)$$

$$S_{nw,m}^* = \frac{S_{nw}^* - S_{nw,r}^*}{1 - A_p} \quad (7)$$

$$S_{nw,r}^* = A_p S_{nw,i}^* \quad (8)$$

$$S_{nw}^* = \frac{S_{nw}}{1 - S_{wi}} \quad (9)$$

where  $P_{c,j}^I$  is the imbibition hysteretic capillary pressure of each voxel  $j$ ,  $S_{nw,m}^*$  is the effective mobile nonwetting phase (CO<sub>2</sub>) saturation, and  $S_{nw}^*$  is the effective nonwetting phase saturation. In Eq. (5),  $\alpha$  is the same scaling factor as in the drainage case and  $P_s$  is the imbibition snap-off capillary pressure. In Eq. (6),  $S_{w,i}^* = 1 - S_{nw,i}^*$ , where  $S_{nw,i}^*$  is the effective initial CO<sub>2</sub> saturation prior to imbibition, a.k.a. the turning point saturation. In Eq. (7),  $S_{nw,m}^*$  is computed using a linear trapping relationship, which is defined in Eq. (8), where  $A_p$  is the pore-scale linear trapping coefficient and  $S_{nw,r}^*$  is the effective residual nonwetting phase saturation. Finally, Eq. (9) shows how the effective nonwetting phase saturation is computed. Instead of using the linear trapping relationship to calculate  $S_{nw,m}^*$ , it is also possible to use the Land trapping relationship, as shown in Eqs. (10) to (12), where  $C_p$  is the pore-scale Land

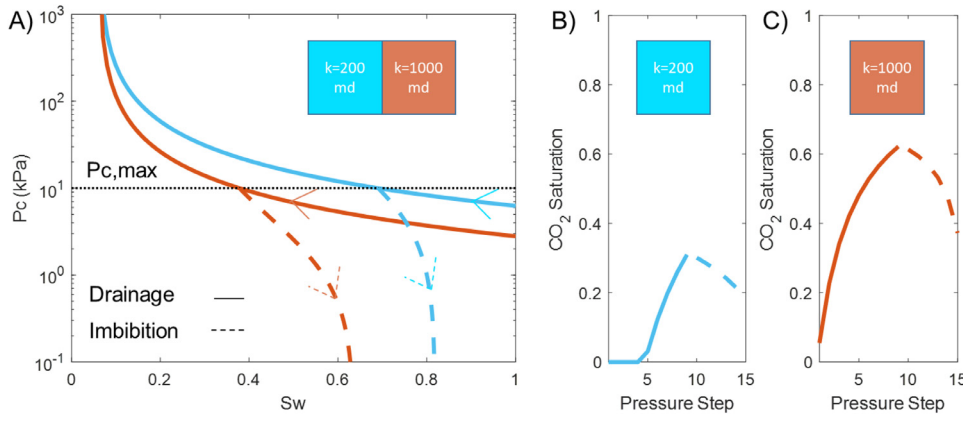


**Fig. 1.** Illustration showing heterogeneous saturation for both drainage and imbibition when at capillary equilibrium for two voxels with different permeability values. A: Capillary pressure curves; Pc: capillary pressure; Sw: water saturation. The arrows indicate the direction of capillary pressure change. Pc, max: The maximum Pc reached during the MP simulation. B, C: CO<sub>2</sub> saturation values at different Pc steps during both drainage and imbibition.

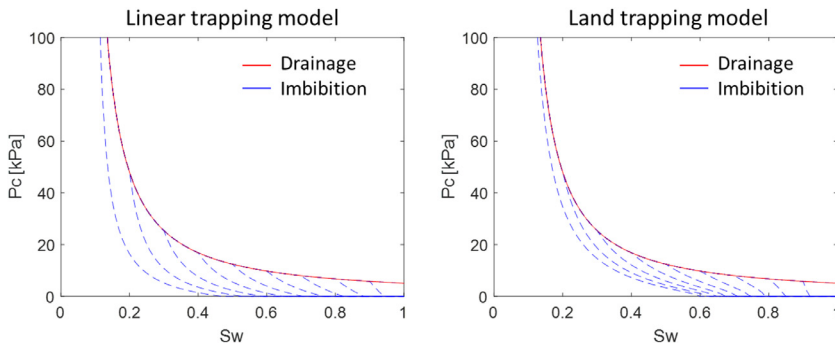


**Fig. 2.** Illustration of the voxel-level capillary pressure model for both drainage and imbibition when  $P_s = 0$ . Left: linear trapping model. Right: Land trapping model. Dashed lines are imbibition hysteretic scanning curves.

trapping coefficient (Jackson et al., 2020; Land, 1968; Pini and Benson, 2017). The illustration for the voxel-level capillary pressure curves is shown in Fig. 2. Fig. 2 also shows the differences between the capillary pressure models computed with the two different trapping models. The selection of the voxel-level residual trapping there exists in the voxel at different capillary pressure values, and will therefore affect the final domain residual trapping amount simulated.

$$S_{nw,m}^* = \frac{1}{2} \left( -\Delta + \sqrt{\Delta^2 - \frac{4\Delta}{C_p}} \right) \quad (10)$$

$$\Delta = S_{nw,r}^* - S_{nw}^* \quad (11)$$

$$S_{nw,r}^* = \frac{S_{nw,i}^*}{1 + C_p S_{nw,i}^*} \quad (12)$$

## 2.2. Simulation procedure

There are three main steps in the MP simulation procedure as illustrated in the workflow chart in Fig. 3: 1) assign simulation input values, 2) conduct the drainage process, and 3) conduct the imbibition process. Previously Section 2.1 has introduced the voxel-level inputs required and how pore-scale residual trapping is accounted for by incorporating hysteresis into the voxel-level input model. The current section will focus on the two-phase flow rules implemented to carry out the drainage and imbibition processes, as well as the macroscopic trapping rules used to account for capillary heterogeneity trapping. For a detailed description of the MP simulation code, see supplementary material.

### 2.2.1. Drainage

A nonzero pressure is imposed on the nonwetting phase to initiate the drainage displacement process. Because there is essentially no viscous pressure gradient, the externally imposed non-wetting phase pressure

is directly equal to the capillary pressure between the two fluids. And because all voxels are at capillary equilibrium, the whole grid therefore has the same capillary pressure everywhere that is equal to the externally imposed nonwetting phase pressure (Ioannidis et al., 1996). For these simulations, the externally imposed nonwetting phase pressure is increased from 0 to a maximum value in small pressure increments of  $\approx 100$  Pa to model the drainage process in which CO<sub>2</sub> invades the fully water-saturated grid. During drainage, for strongly water-wet porous media, under capillary dominated flow regimes, the nonwetting phase cannot enter the domain unless the capillary entry pressure is overcome. Therefore, invasion percolation algorithm is used to simulate the drainage process. This results in a distinct CO<sub>2</sub> invasion front as shown in Fig. 4 (Ioannidis et al., 1996; Kueper and McWhorter, 1992; Wilkinson and Willemsen, 1983). As shown in the workflow chart in Fig. 3, at each pressure step, the simulator examines which voxels on the CO<sub>2</sub> invasion front have capillary entry pressures lower than the currently imposed pressure, and will invade those voxels if that is the case. Then the CO<sub>2</sub> saturation values of the invaded voxels are computed using the capillary pressure functions defined for each voxel (Kueper and McWhorter, 1992). Therefore, the front can only advance through the domain if the capillary pressure is greater than the entry pressure of the voxels downstream of the invasion front.

### 2.2.2. Imbibition

After the drainage process is complete, the imposed pressure is then reduced in the same number of pressure steps from the maximum drainage capillary pressure back to 0 to model the imbibition process in which water displaces CO<sub>2</sub>. The imbibition process is terminated when the CO<sub>2</sub> saturation field reaches a constant value because the remaining CO<sub>2</sub> is trapped. We assume that water can flow throughout the entire domain in grain-coating films for strongly water-wet porous media. Therefore, an ordinary percolation algorithm is suitable to model imbibition at the continuum scale because it allows water to get access to the whole domain at any capillary pressure. As a consequence, no water imbibition

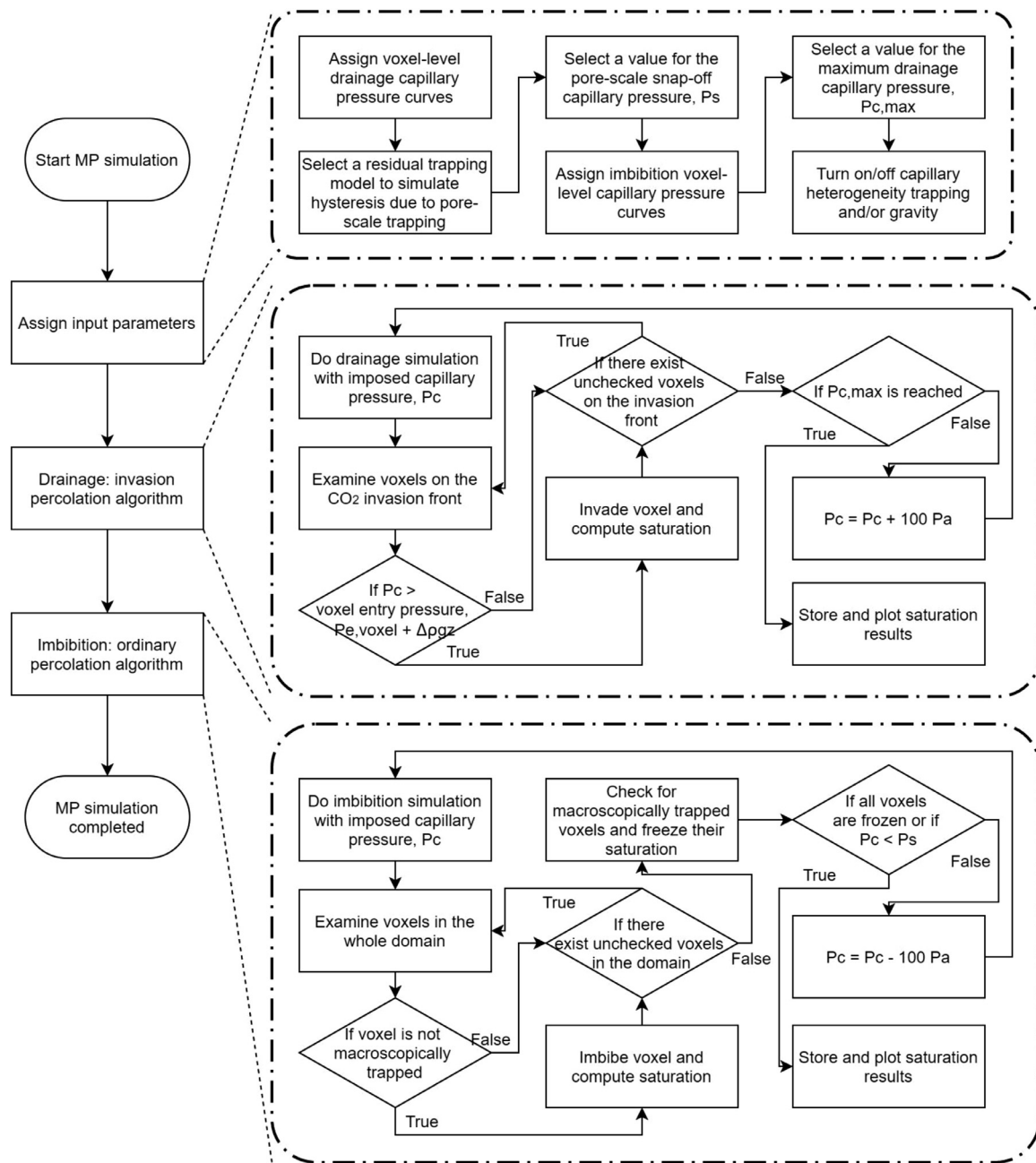


Fig. 3. MP simulation workflow chart. Both gravity and CO<sub>2</sub> capillary heterogeneity trapping are turned on in this illustration.

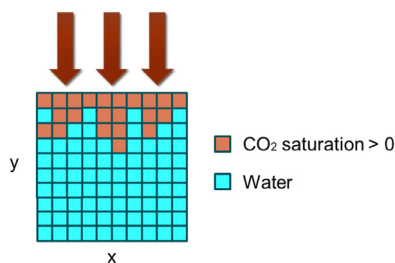


Fig. 4. Drainage simulation schematic shown for a low capillary pressure value: CO<sub>2</sub> invades from the inlet in an invasion percolation style. Note that the CO<sub>2</sub> invaded region has a single capillary pressure value of some finite value greater than zero, and the water saturated region has a single capillary pressure value of zero.

front is observable, as demonstrated in Fig. 5 (Ioannidis et al., 1996). When no capillary heterogeneity trapping is accounted for, the saturation of each voxel is simply calculated according to the individually defined voxel-level imbibition hysteretic capillary pressure functions at each pressure step.

### 2.2.3. Implementation of capillary heterogeneity trapping

During MP drainage simulation, because it is assumed that water dominantly flows in films, no water capillary heterogeneity trapping by CO<sub>2</sub> invasion is imposed. The justification for this simulation choice is that water flowing in films means that the wetting phase is always continuous in the domain so CO<sub>2</sub> should not be able to disconnect any portion of water from the continuous water phase at any capillary pressure. Therefore, given a high enough capillary pressure, CO<sub>2</sub> is capable of invading all voxels to the irreducible water saturation as shown in Fig. 6 (left).

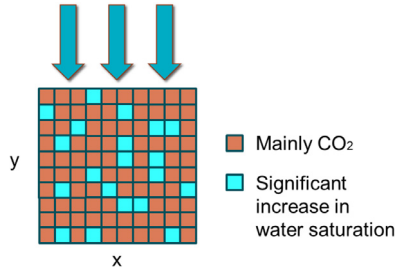


Fig. 5. Imbibition simulation schematic shown for a high capillary pressure value: water imbibes from the inlet in an ordinary percolation style.

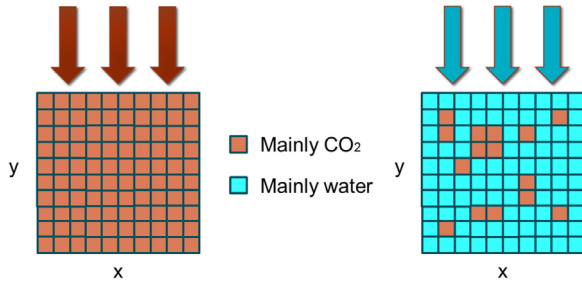


Fig. 6. Trapping schematic shown for drainage at a high maximum capillary pressure value (left): CO<sub>2</sub> invades the whole grid at the end of drainage; trapping schematic shown for imbibition (right): CO<sub>2</sub> trapped by macroscopic trapping rules at the end of imbibition is shown by the CO<sub>2</sub> filled orange voxels surrounded by water-filled blue voxels.

During MP imbibition simulation, while CO<sub>2</sub> pore-scale trapping is captured by hysteresis in the voxel-level capillary pressure curves, in order to capture CO<sub>2</sub> capillary heterogeneity trapping caused by mesoscale heterogeneity, two macroscopic trapping rules are implemented. The first imbibition macroscopic trapping rule states that when a group of voxels is completely surrounded by neighboring voxels at their voxel-level residual saturation then this group of voxels is determined to be macroscopically trapped by the capillary heterogeneity trapping mechanism. The CO<sub>2</sub> saturation value of the macroscopically trapped voxels can no longer change with decreasing capillary pressure, as shown in Fig. 6 (right) (Ioannidis et al., 1996; Kueper and McWhorter, 1992; Yortsos et al., 1993). With this trapping rule, CO<sub>2</sub> tends to be trapped in higher permeability regions, which have lower capillary entry pressure and are surrounded by lower permeability regions, which require higher capillary entry pressure to enter.

With only the first macroscopic trapping rule applied, the match in voxel-level CO<sub>2</sub> saturation between MP and full-physics simulation results is good for a low degree of heterogeneity, but at a high degree of heterogeneity, MP simulation consistently underestimates the trapped CO<sub>2</sub> saturation. Therefore, a second macroscopic trapping rule needs to be applied. This second rule states that all voxels are macroscopically trapped when the domain capillary pressure value drops below the imbibition snap-off capillary pressure. This is because at or below this snap-off capillary pressure value, CO<sub>2</sub> is no longer a continuous phase and should not be able to flow. As shown in the workflow chart in Fig. 3, with both macroscopic trapping rules applied, now for imbibition, it is necessary to first check whether the current capillary pressure is high enough and whether the voxels are macroscopically trapped before proceeding.

After the imbibition process is finished, simulation of a single primary drainage and secondary imbibition cycle is now complete. The domain effective CO<sub>2</sub> saturation can then be calculated at each pres-

sure step and the domain effective capillary pressure curves for both drainage and imbibition can be obtained. By convention, capillary pressure graphs show the difference in pressure between the two continuous immiscible phases plotted against water saturation, because this is the only capillary pressure that is measurable in Darcy-scale lab experiments. In the MP simulation case, this would be equivalent to plotting the externally imposed pressure against the water saturation (Ioannidis et al., 1996; Yortsos et al., 1993). However, it is worth noting that the externally imposed pressure (capillary pressure of the continuous phases) is not simply equal to the average capillary pressure of the grid (simple arithmetic average of voxel-level capillary pressure values at each effective water saturation). This is especially the case before CO<sub>2</sub> percolation during drainage and when there is CO<sub>2</sub> capillary heterogeneity trapping during imbibition.

#### 2.2.4. Implementation of gravity in the MP simulator

The MP simulator is capable of incorporating gravity forces by imposing capillary-gravity equilibrium. When the domain size is small, gravity effects are much smaller than capillary effects and can be ignored. However, for large domain sizes such as the field scale, it is important to consider gravity forces. When gravity forces are ignored, the MP simulator does not require specifying the exact size of the voxel. However, when gravity forces are considered, the voxel size in the vertical *z* direction does need to be supplied for the MP simulator to calculate the difference in hydrostatic head between voxel pairs.

When gravity forces are not added, the imposed capillary pressure  $P_{c,imposed}$  of the whole domain is

$$P_{c,imposed} = P_{CO_2} - P_w \quad (13)$$

where  $P_{CO_2}$  and  $P_w$  are the pressure in the CO<sub>2</sub> and the water phase respectively. When gravity forces are included in the model, there exists a hydrostatic pressure gradient in both the CO<sub>2</sub> and the water phase as shown in Fig. 7A. The capillary pressure of the domain can then be computed as follows (Ioannidis et al., 1996).

$$P_{c,dz=0} = P_{CO_2,dz=0} - P_{w,dz=0} = P_{c,imposed} \quad (14)$$

$$P_{c,dz} = P_{CO_2,dz} - P_{w,dz} = P_{c,imposed} - \Delta\rho g dz \quad (15)$$

Gravity forces are calculated as  $\Delta\rho g dz$ , where  $\Delta\rho$  is the density difference between the two fluids (water and CO<sub>2</sub>),  $g$  is the gravitational acceleration, and  $dz$  is the relative depth defined as 0 at the top of the domain and increases to the maximum value at the bottom of the domain as shown in Fig. 7A. From Eqs. (14) and (15), it is apparent that when gravity forces are present, the effective capillary pressure value decreases with the depth  $dz$  in the domain. With gravity forces added, now a voxel can only be invaded during drainage when the currently imposed domain capillary pressure is greater than the capillary entry pressure of the current voxel and the gravity forces combined as shown in Eq. (16).

$$P_{c,dz} > P_{e,voxel}, \text{ or equivalently, } P_{c,imposed} > P_{e,voxel} + \Delta\rho g dz \quad (16)$$

Fig. 7B and C show the capillary pressure values needed to invade each voxel in a realistic reservoir slice domain with and without gravity forces added. Details of this domain will be presented later in Section 2.3.3. For an invading fluid (CO<sub>2</sub>) that is lighter than the defending fluid (water), gravity forces hinder downward fluid invasion (Ioannidis et al., 1996). This can be clearly seen by comparing the two graphs, as much higher pressure is needed in order to invade deeper voxels.

#### 2.3. Simulation input data

This section provides the values used for the voxel-level inputs and explains the two sets of simulation cases run with the MP simulator. The first set of MP simulation cases is run to obtain the domain-specific CO<sub>2</sub>

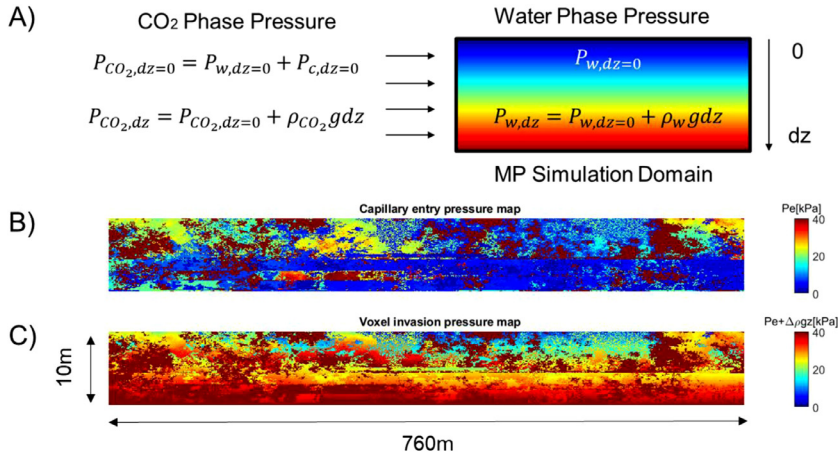


**Fig. 7.** Gravity forces illustrations. A: Capillary-gravity equilibrium computation illustration showing the CO<sub>2</sub> phase migrating into the MP simulation domain from the left edge. dz: relative depth. P: pressure.  $\rho$ : density. Color: hydrostatic pressure gradient. B: Capillary entry pressure map of a realistic reservoir slice. C: Voxel invasion pressure map that combines the voxel entry pressure and the hydrostatic pressure gradient on the same reservoir slice.

**Table 1**  
Values of voxel-level input parameters.

Parameter	Value
Core average porosity $\phi_{avg}$	0.19
Voxel-level porosity $\phi_i$	0.19
Mean permeability $k_{avg}$	300 md
Irreducible water saturation $S_{wi}$	0.06
Pore size distribution index $\lambda$	0.85
CO <sub>2</sub> /water capillary entry pressure $P_e$ for the Brooks-Corey model for mean permeability	5.1 kPa
Pore-scale linear trapping coefficient $A_p$	0.46
Normalized pore-scale Land trapping coefficient $C_p$	1.3
Snap-off capillary pressure $P_s$	$P_e$

residual trapping abilities for different types and degrees of mesoscale heterogeneity. The second set is run on a realistic vertical reservoir slice to demonstrate how the MP simulator can be applied at the field scale.

In order to ensure that saturation is sufficiently uniform within a voxel to be represented by a single value, both viscous and gravity forces need to be small relative to capillary forces within the voxel. Therefore, the voxel size cannot be arbitrary and needs to be small enough to ensure that the MP simulation assumptions are valid. While viscous forces mainly act on CO<sub>2</sub> in the horizontal direction in a vertical well injection scenario, gravity forces only act on CO<sub>2</sub> in the vertical direction. Therefore, we would expect the magnitude of the viscous forces to limit the size of the voxel in the horizontal direction and the magnitude of the gravity forces to limit the size of the voxel in the vertical direction. The voxel size selected for the core-scale analysis is 2 mm, which is well below the voxel size limit at which viscous forces ( $kP_e/\mu\nu \approx 0.3$  m) and gravity forces ( $P_e/\Delta\rho g \approx 0.7$  m) surpass capillary forces (Ioannidis et al., 1996). The voxel size selected for the field-scale analysis is 1 m in the horizontal direction and 5 cm in the vertical direction. While the vertical voxel size is well within the limit of 1.3 m, the horizontal voxel size limit varies between 0.8 m and 1400 m largely depending on the flow rate  $\nu$  chosen. Even so, the horizontal voxel size is approximately at the strictest limit of 0.8 m. With this field-scale voxel size, the macroscopic Bond number ( $\Delta\rho g l/P_{e,d}$ ) is  $10^{-2}$ , where  $l$  is the voxel height, and  $P_{e,d}$  is the domain effective entry (breakthrough) capillary pressure (Ioannidis et al., 1996). See supplementary material for calculation details.

### 2.3.1. Voxel-level input data

In order to use the Leverett J-function scaling relationship to assign voxel-level capillary pressure curves as inputs into the MP simulator, voxel-level porosity and permeability values need to be specified. For this study, a constant porosity value is assigned to all the voxels for simplicity as is done in Li and Benson (2015). Table 1 shows the voxel-level input parameter values used. The values for the various input parameters are based on the average Berea sandstone experimental data pub-

lished by Krevor et al. (2012) and Ni et al. (2019). One exception is the pore-scale linear trapping coefficient,  $A_p$ .

In order to obtain a sandstone rock's residual trapping characteristics, coreflooding experiments need to be conducted, upon the results of which, empirical trapping relationships such as the linear or the Land models are fitted. Due to the fact that the medical CT scanners do not provide micron-level resolution, it is not possible to directly differentiate between pore-scale and mesoscale residual trapping mechanisms. Consequently, the experimental residual trapping models capture all residual trapping regardless of the underlying trapping mechanisms. The MP simulation addresses this challenge by explicitly simulating the two residual trapping mechanisms separately. Because the macroscopic trapping rules separately account for capillary heterogeneity trapping, the trapping model for voxel-level hysteresis should strictly capture only pore-scale residual trapping.  $A_p$  is the coefficient in the linear trapping model defined in Eq. (8), and Ni et al. (2019) have used an extrapolation method to infer the  $A_p$  value on a set of diverse coreflooding data. Therefore, the resulting value of  $A_p = 0.46$  is used as the input in the MP simulation model for voxel-level hysteresis. Just like the  $P_s$  parameter, this input  $A_p$  value significantly affects the MP residual trapping simulation results. Therefore, a sensitivity study on the value of this input parameter can be found in Appendix A.

### 2.3.2. Trapping ability simulation input data

We can employ the MP simulator to quickly obtain post-imbibition CO<sub>2</sub> residual trapping ability for different types of domains by turning on capillary heterogeneity trapping. All simulation cases in this section have 3D cubic domains the size of  $10 \times 10 \times 10$  voxels with artificially generated permeability fields. The voxel size used is  $2 \text{ mm} \times 2 \text{ mm} \times 2 \text{ mm}$ , which is greater than the representative elementary volume scale (Jackson et al., 2020; Pini and Madonna, 2016). Because the domain size is small, gravity forces do not have a significant influence and are turned off for this set of simulation cases. The inlet face is to the left and the outlet face is to the right. The permeability fields used can be completely random or homogeneous except for a downstream low per-

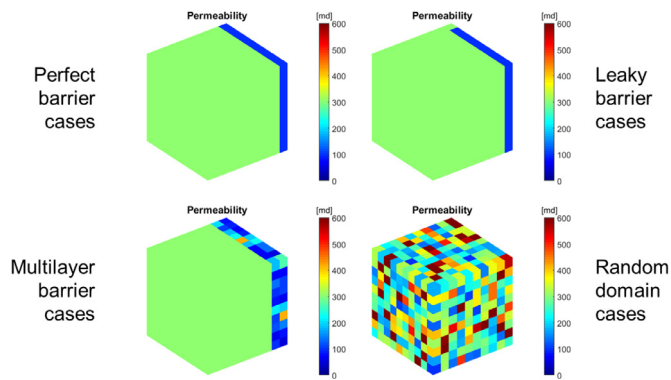


**Fig. 8.** Illustration of the four types of domains investigated: the perfect barrier case, the leaky barrier case, the multilayer barrier case, and the random domain case.

meability barrier, as shown in Fig. 8. The random permeability fields are uncorrelated with a lognormal distribution. For the random permeability fields, the permeability value for each voxel is randomly generated from a normal distribution with a specified mean and standard deviation. An increasing standard deviation represents an increasing spread of the permeability values and this in turn represents an increasing degree of mesoscale heterogeneity. After a normal distribution is obtained, the values are exponentiated in order to get lognormally distributed permeability values. For the permeability fields with barriers, there are three types of barriers that are investigated. The perfect barrier type has a single layer of voxels with homogeneous, low permeability values. The leaky barrier type has a “hole” the size of a single voxel in the upper corner of its barrier, and is otherwise identical to the perfect barrier. Finally, the multilayer barrier type has two layers of barrier voxels with lognormally distributed uncorrelated random low permeability values with a standard deviation ( $\text{std}(\ln(k))$ ) of 0.5.

For random domains, we want to investigate how increasing the degree of heterogeneity affects the domain effective linear trapping coefficient,  $A_d$ . So ten random domains with different values of  $\text{std}(\ln(k))$  ranging from 0 to 5 are used, where 5 represents an extremely high degree of mesoscale heterogeneity. For barrier domains, we want to investigate how increasing the permeability contrast between the upstream domain and the downstream capillary barrier affects  $A_d$ . So eleven barrier domains with different values of the downstream low permeability barrier are used. A fifth type of domain with an extremely high degree of heterogeneity is also examined. For the extreme cases, we position 5 layers of homogeneous barrier downstream. The permeability values of the extreme case barriers are quite low. Note that the input mean or upstream domain permeability into the simulation is always at 300 md for every case.

Previously in literature, it has been assumed that the capillary dominated residual trapping relationship for a certain rock type does not change across scales and it is considered an intrinsic property of the porous medium itself (Al-Menhali and Krevor, 2016; Krevor et al., 2015; Niu et al., 2015; Pini and Krevor, 2019). In order to examine whether the initial-residual saturation (IR) curves are truly scale invariant, for every case in this section, we run twenty MP simulations with different maximum drainage capillary pressure values. Then the linear and Land trapping coefficients computed from the domain averaged initial and residual  $\text{CO}_2$  saturation values are plotted on a single IR plot. We can then compare this domain-level trapping relationship with the voxel-level trapping relationship. All model parameter values covered in this section are shown in detail in Table 2.

### 2.3.3. Field-scale simulation input data

The MP simulator is applied to a realistic vertical reservoir slice domain to predict both post-drainage and post-imbibition  $\text{CO}_2$  saturation.

The reservoir slice is extracted from parasequence-1 of the Paaratte formation at the Otway site in Australia in between well CRC2 and CRC3 (Mishra et al., 2020, 2019). The Paaratte sandstone formation is a saline aquifer (Pevzner et al., 2013). At a depth of 1500 m, the temperature is 60 °C and the pressure is 15 MPa. The dimension of the model is 40 m vertically and 760 m horizontally. The voxel size is 1 m × 1 m × 5 cm with 5 cm as the resolution in the vertical direction. Realistic porosity, permeability, rock type, and facies values have been assigned to the voxels in the model to best represent the true properties of the geological formation (Mishra et al., 2020, 2019). The depositional facies and rock type maps generated are constrained by log data of the two wells present near the two ends of the domain. Therefore the layer thicknesses in the vertical direction are set, ranging from a few centimeters to 5–8 m for different facies. Different variograms have been derived for different facies, and these facies therefore each has a different correlation length in the horizontal direction, ranging from 200–300 m to over a kilometer. Porosity and permeability values are correlated, and are both associated with the facies and rock types assigned. For more details about how the field-scale model is generated, see Mishra et al. (2020, 2019) and Dance et al. (2019).

For the current study, we use a modified version of the aforementioned vertical reservoir slice domain by applying the following simplifications. We choose to ignore the dip angle of 4° in the formation and select only the top 10 m of the domain, which includes roughly 150,000 voxels. The porosity and horizontal permeability maps for the simulation domain are shown in Fig. 9. The domain has an average porosity of 0.21 and a geometric permeability average of 37 md. It can be clearly seen that this is a highly heterogeneous domain, with an  $\text{std}(\ln(k))$  value of 2.8. The resulting pressure required to invade the voxels in this domain with or without gravity present is shown in Fig. 7B and C. The capillary pressure curve for each voxel is calculated using the Leverett J-function scaling relationship in Eqs. (1)–(4) with the properties for  $k_{avg}$ ,  $\lambda$ , and  $P_e$  provided in Table 1. Anisotropy in the permeability field is disregarded and only the horizontal permeability values are used. Finally, the density of water and  $\text{CO}_2$  are uniform throughout the domain based on a temperature of 60 °C and a pressure of 15 MPa ( $\rho_w = 989.60 \text{ kg/m}^3$  and  $\rho_{\text{CO}_2} = 604.09 \text{ kg/m}^3$  (Lemmon et al., 2018)).

Gravity forces are included for this field-scale simulation case. With gravity, the externally imposed capillary pressure value is the greatest at the top layer of the model and reduces with increasing depth for  $\text{CO}_2$  drainage and water imbibition. A maximum capillary pressure value of 35 kPa during drainage is selected. This value is selected such that the domain reaches post-drainage  $\text{CO}_2$  saturation values observed from full physics simulations of  $\text{CO}_2$  injection at flow rates typical for field-scale projects.

For MP simulation boundary conditions, the inlet is the left edge and the outlet is the right edge. Because viscous forces are the strongest at the injection well and reduce rapidly away from the well (Dance et al., 2019; Hovorka et al., 2006; Meckel and Bryant, 2014), the MP simulator is best applied to domains some distance away from the injection well where flow rates are low enough that capillary and gravity forces dominate (Celia et al., 2015; Meckel et al., 2015). Table 3 summarizes all the model parameter values for this field-scale domain.

## 3. MP simulation results and discussion

There are two major parts to the results. The first part of this section shows and discusses the  $\text{CO}_2$  residual trapping ability simulation results for the four different types of synthetic cube domains. The second part of this section applies the MP simulator to a realistic fine-grid vertical reservoir slice domain.

### 3.1. Trapping ability simulation results

Before we report the trapping abilities for the different types of permeability fields, we first turn our attention to the difference between

**Table 2**  
Values of all model input parameters for the different cases of synthetic cube domains.

	Perfect barrier case	Leaky barrier case	Multilayer barrier case	Random domain case	Perfect-extreme barrier case
Domain size	10 × 10 × 10 voxels				
Voxel size	2 mm × 2 mm × 2 mm				
Gravity forces	Off				
Flow direction	Left to right				
Number of downstream barrier layers	1	1	2	0	5
Barrier permeability mean	{250, 200, 150, 100, 60, 30, 10, 3, 0.3, 0.01, 0.001} md			–	{0.3, 0.01, 0.001} md
Barrier std(ln(k))	–	–	0.5	{0, 0.35, 0.5, 0.75, 1, 1.5, 2, 2.5, 3, 5}	–
MP simulation maximum drainage capillary pressure	{1000, 2000, 3000, 4000, 5000, 6000, 7000, 8000, 9000, 1e4, 1.1e4, 1.2e4, 1.5e4, 2e4, 3e4, 4e4, 5e4, 1e5, 2e5, 1e6} Pa				

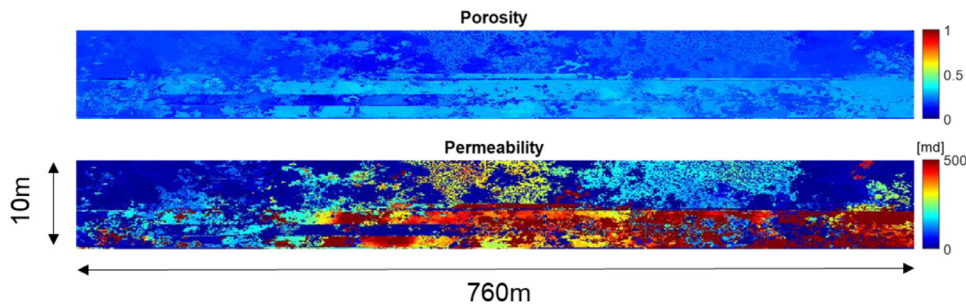


**Fig. 9.** Porosity and permeability maps for the vertical reservoir slice.

**Table 3**  
Summary of the model parameter values for the case of field-scale domain.

Model parameter	Parameter value
Domain size	760 m × 1 m × 10 m
Voxel size	1 m × 1 m × 5 cm
Gravity forces	On
Formation top depth	1500 m
Formation temperature	60 °C
Formation pressure	15 MPa
Average porosity	0.21
Permeability geometric mean	37 md
Permeability std(ln(k))	2.8
Water density	989.60 kg/m <sup>3</sup>
CO <sub>2</sub> density	604.09 kg/m <sup>3</sup>
MP simulation maximum drainage capillary pressure	35 kPa
Flow direction	Left to right

the voxel-level and the domain-level residual trapping relationships as shown in Fig. 10. Fig. 10 displays the voxel-level and domain-level IR plots with different voxel-level trapping models for the same domain that has uncorrelated random permeability values. Here the voxel-level IR plot is obtained by simulating a single primary drainage/imbibition cycle and plotting the voxel-level IR values, whereas the domain-level IR plot is obtained by simulating repeated primary drainage/imbibition cycles and plotting the domain effective IR values.

From the voxel-level IR plots, in the case when  $P_s$  is nonzero, it can be seen that voxels with low initial CO<sub>2</sub> saturation (<0.4) follow the input voxel-level trapping relationships ( $P_s = 0$ ), and voxels with high initial CO<sub>2</sub> saturation (>0.4) display capillary heterogeneity trapping behaviors that diverge from the input voxel-level trapping relationships. The permeability of the voxels at which this apparent “bend” occurs is approximately at the domain median permeability value. Similar voxel-level IR results can also be found in full-physics coreflooding simulations conducted by Jackson and Krevor (2019). The reason for this kind of trapping behavior is as follows. Low permeability voxels, according to the Leverett-J scaling relationship, will have voxel-level capillary pressure curves with high capillary entry pressure. This means that in the post-drainage CO<sub>2</sub> saturation field at capillary equilibrium,

these low permeability voxels will have low initial CO<sub>2</sub> saturation. Then during the MP imbibition simulation process as the domain capillary pressure decreases, these low permeability voxels will reach their pore-scale residual trapping amount first and get frozen. As the imbibition capillary pressure keeps dropping, only after the domain already contains frozen voxels can other higher permeability voxels have a chance of been macroscopically trapped. As a consequence, capillary heterogeneity trapping behavior occurs only in higher permeability voxels, which have low capillary entry pressures and high drainage CO<sub>2</sub> saturations.

From the domain-level IR plots, it can be seen that with the linear trapping model as the voxel-level input, the macroscopic trapping rules cause the domain-level IR curve to deviate from the linear trapping model and follow a double linear model. A linear trapping relationship similar to the double linear model shown here has been reported on a water-wet limestone using the porous plate experimental method (Tanino and Blunt, 2013). This double linear trapping model is a direct consequence of the first macroscopic trapping rule implemented. The effect of this trapping rule is such that if imbibition proceeds before CO<sub>2</sub> drainage has percolated the domain (reached the outlet), then any CO<sub>2</sub> present in the domain will be 100% trapped at the end of imbibition. Such trapping behavior is realistic and has been observed in sand tank experiments (Trevisan et al., 2017b). Only after CO<sub>2</sub> drainage has percolated the domain can the effect of the pore-scale residual trapping model be seen at the domain level after imbibition.

Fig. 10 clearly shows that regardless of the type of voxel-level trapping model implemented, there are significant differences between the input voxel-level trapping model and the larger-scale domain effective trapping relationship. This MP simulation result shows that residual trapping relationships are not scale invariant when capillary heterogeneity trapping is present.

In order to investigate how residual trapping abilities vary with different types and degrees of mesoscale heterogeneity, MP simulations are run on four types of permeability fields with varying degrees of heterogeneity or matrix-barrier permeability contrast. In order to measure the linear trapping coefficient for any domain more accurately, the fitted least square linear regression values are reported in this section. However, note that with this fitting, the linear residual trapping ability will

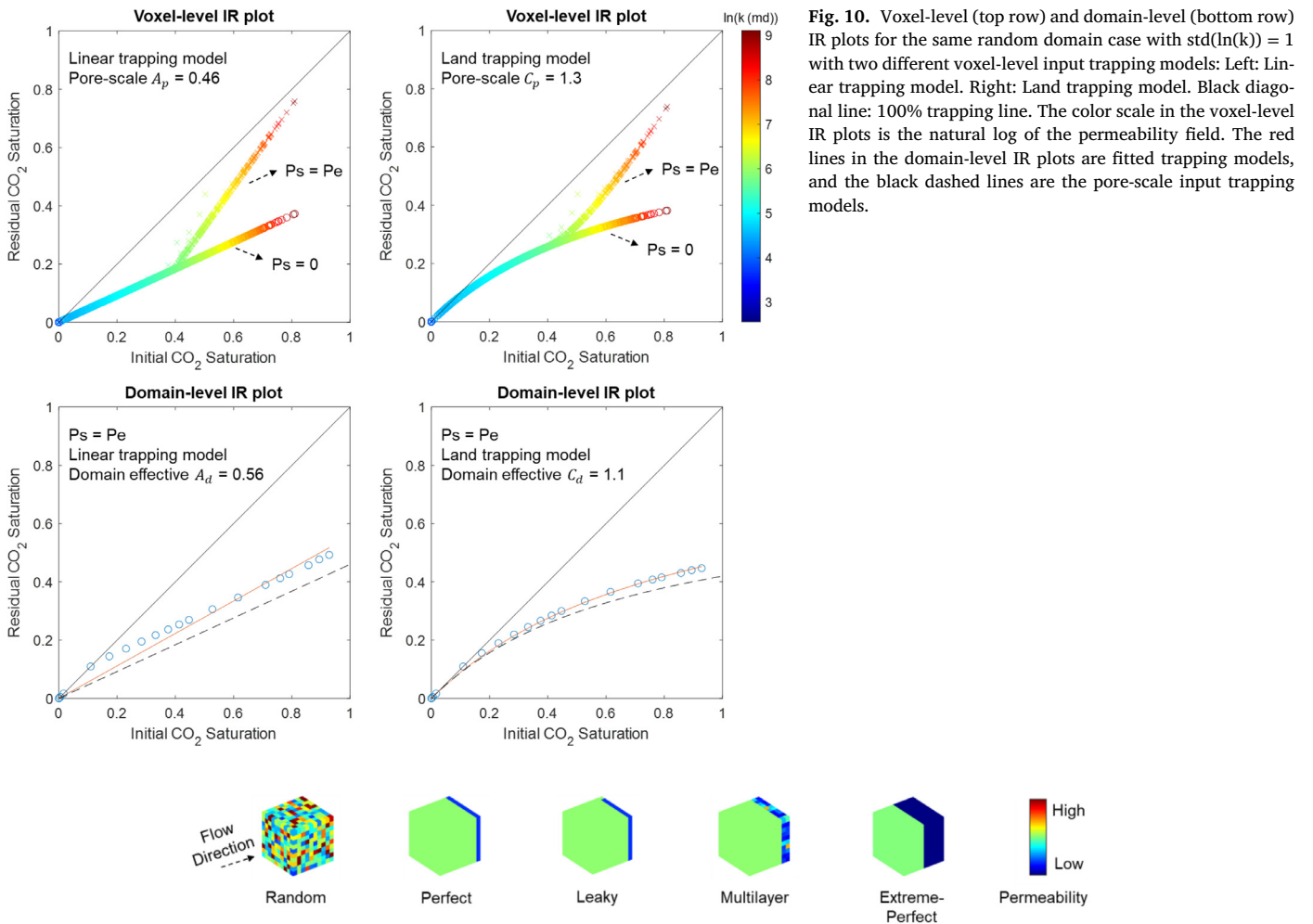


Fig. 10. Voxel-level (top row) and domain-level (bottom row) IR plots for the same random domain case with  $\text{std}(\ln(k)) = 1$  with two different voxel-level input trapping models: Left: Linear trapping model. Right: Land trapping model. Black diagonal line: 100% trapping line. The color scale in the voxel-level IR plots is the natural log of the permeability field. The red lines in the domain-level IR plots are fitted trapping models, and the black dashed lines are the pore-scale input trapping models.

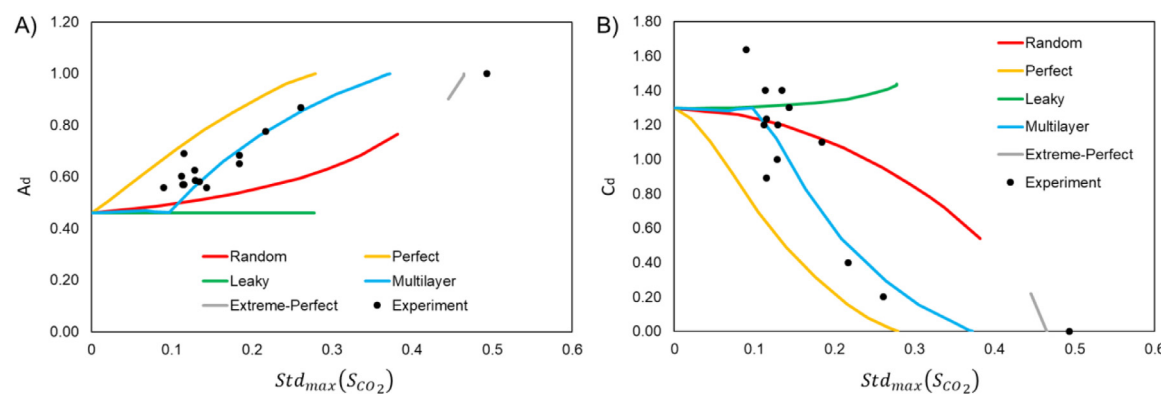
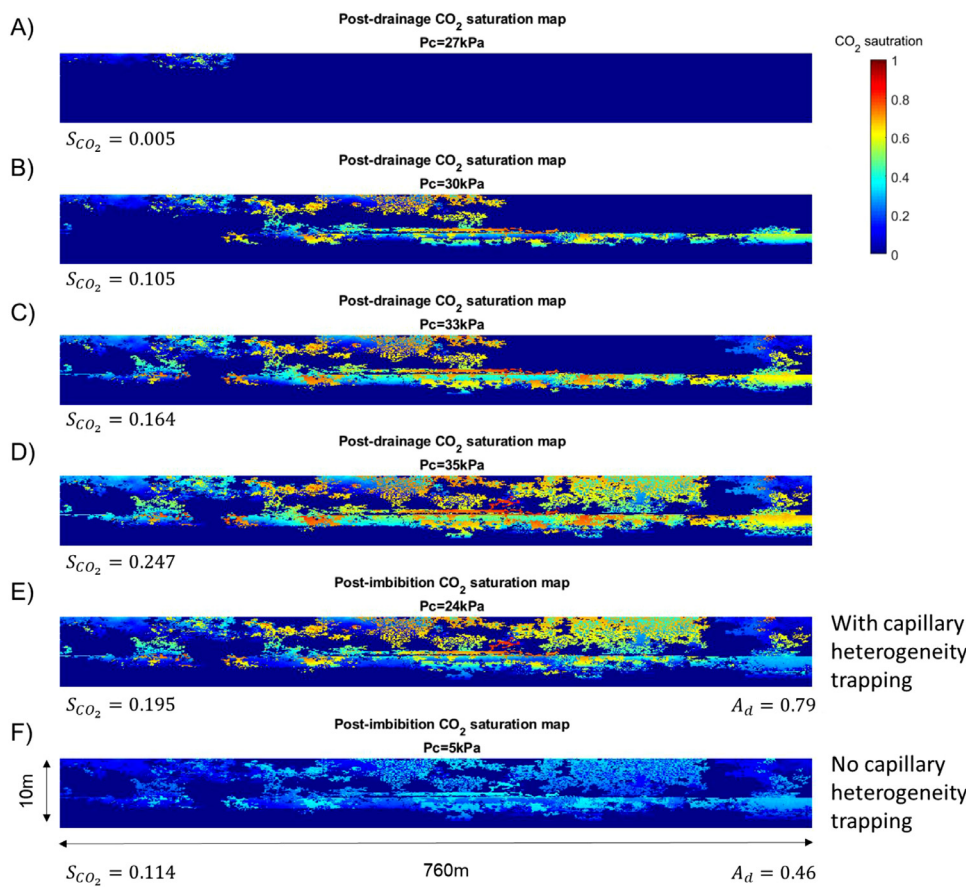


Fig. 11. All MP simulation results for the trapping ability simulation cases and previous experimental results with different voxel-level input trapping model: A: linear trapping model; B: Land trapping model (Krevor et al., 2012, 2011; Ni et al., 2019; Reynolds et al., 2018). Images of the permeability fields of the different synthetic cube domains are shown at the top. Refer to Section 2.3.2 for a detailed description of the different heterogeneous models.

be underestimated when the initial saturation is low and overestimated when the initial saturation is high.

Fig. 11 shows all simulation results with two different voxel-level input residual trapping models, the linear trapping model in A and the Land trapping model in B. From Fig. 11A, we can see that other than the leaky barrier case, the domain effective linear trapping coefficient,  $A_d$ , increases with the degree of mesoscale heterogeneity represented by the maximum standard deviation in the drainage CO<sub>2</sub> saturation fields,  $\text{std}_{\max}(S_{CO_2})$ . This simulation result is consistent with the experimental results shown in black dots. This result is also consistent with simulation

results in the literature, that under capillary dominated flow regimes, more oil capillary heterogeneity trapping can be achieved in water-wet rocks with increasing permeability contrasts for cross-lamination flow (Corbett et al., 1992). However, unlike previously assumed, the relationship between  $A_d$  and  $\text{std}_{\max}(S_{CO_2})$  appears to be nonlinear and dependent on the structure of the heterogeneity field. For the multilayer barrier case, no extra capillary heterogeneity trapping can be achieved at low degrees of heterogeneity. Yet as the degree of heterogeneity increases, the multilayer barrier domain has a similar shape with the perfect barrier case and it is also the case that best fits the experimental



**Fig. 12.** The CO<sub>2</sub> saturation maps of six capillary pressure steps taken during drainage and imbibition. A – D: drainage. D: drainage end state reached at the maximum capillary pressure. E: imbibition end state with capillary heterogeneity trapping. F: imbibition end state with no capillary heterogeneity trapping.

data. For the leaky barrier case, it is clear that when the capillary barrier is leaky, no capillary heterogeneity trapping can be achieved even at a high degree of heterogeneity. As shown in Fig. 11B, similar trends in the residual trapping results can be obtained when the voxel-level input trapping model changes from the linear to the Land model.

The simulation results from these four different types of domains have demonstrated that although these domains can have the same degree of mesoscale heterogeneity by this simple standard deviation measure, the actual residual trapping ability value is highly heterogeneity dependent. Good capillary barriers can achieve a much higher residual trapping ability at a lower degree of heterogeneity than an uncorrelated random domain. A good fit of the multilayer barrier case to the majority of the experimental data also suggests that some sandstone rock samples used here may in fact be mostly homogeneous with just a few capillary barriers to be able to achieve a high amount of capillary heterogeneity trapping. Numerical values of the data used in Fig. 11 can be found in supplementary material.

However, we notice that there is one experimental data point shown in Fig. 11 with an extremely high degree of heterogeneity that cannot be simulated by the aforementioned four types of domains. For the random domains,  $\text{std}(\ln(k)) = 5$  already represents an extremely high degree of heterogeneity and further increases in  $\text{std}(\ln(k))$  are possible but not realistic. For the barrier domains, reducing the barrier permeability below 0.01 md no longer increases the degree of heterogeneity value measured by the parameter  $\text{std}_{\max}(S_{CO_2})$ . In an effort to simulate the data point with an extremely high degree of heterogeneity, the fifth type of extreme barrier cases is run. The results are close to the data point albeit still being slightly less heterogeneous by the  $\text{std}_{\max}(S_{CO_2})$  measure.

Sensitivity analysis run with different values of the  $P_s$  and the  $A_p$  parameter show that although the resulting  $A_d$  values do vary, the general trends as shown in Fig. 11 remain the same. It is worth noting that

even as we vary the two input parameters, the two domains with the nonleaky downstream barriers remain the most consistent with the experimental data points. This result indicates that real sandstone rocks behave more closely to the two nonleaky barrier domains than the random or the leaky barrier domains. For the sensitivity analysis results, see supplementary material.

### 3.2. Field-scale simulation results

The results of the vertical slice MP simulation are shown in Figs. 12 and 13. Fig. 12 shows the CO<sub>2</sub> saturation results of several pressure steps taken during drainage and imbibition. Fig. 12 also shows the end states for both drainage and imbibition with and without capillary heterogeneity trapping. Fig. 13 shows the corresponding voxel-level capillary pressure curves for the two different imbibition end states shown in Fig. 12.

From Fig. 12, it can be seen that during drainage there exists a distinct invasion front extending from the inlet on the left to the outlet on the right as the domain capillary pressure increases. Similarly heterogeneous plume saturation caused by capillary heterogeneity have been observed in modeling studies by Jackson and Krevor (2020). After the CO<sub>2</sub> plume percolates through the domain, CO<sub>2</sub> continues to invade more voxels as domain capillary pressure further increases and backfills towards the lower parts of the domain in the presence of gravity. The backfilling would be more obvious if the maximum capillary pressure value reached during drainage is set higher. We can also see that no distinct imbibition front is present as the domain capillary pressure drops during imbibition. The CO<sub>2</sub> plume in the domain becomes fully immobilized when the externally imposed capillary pressure reduces to 24 kPa when capillary heterogeneity trapping is included as shown in Fig. 12E. With capillary heterogeneity trapping excluded, the plume continues to

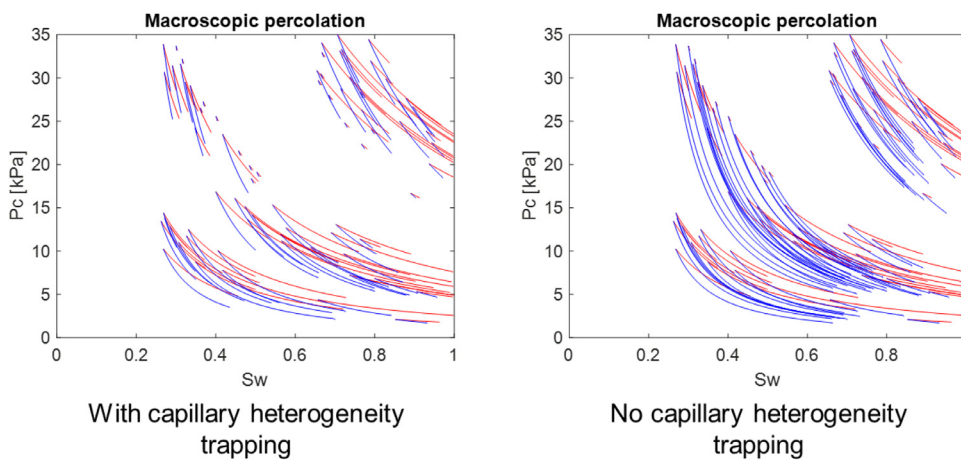


**Fig. 13.** Capillary pressure simulation results for a subset of the voxels in the field scale MP simulation. Left: With capillary heterogeneity trapping. Right: With no capillary heterogeneity trapping. Red lines: every 1000th voxel-level drainage curves. Blue lines: every 1000th voxel-level imbibition curves.

migrate until the externally imposed capillary pressure reduces to the imbibition snap-off value of 5 kPa as shown in Fig. 12F.

When the end state is reached after drainage in Fig. 12D, we can see that the post-drainage  $\text{CO}_2$  saturation at some regions can be as high as 0.8, although the majority of invaded voxels have  $\text{CO}_2$  saturation values lower than 0.6. High  $\text{CO}_2$  saturation values (0.6 – 0.8) in thin layers of plume have been observed away from the injection well in field-scale  $\text{CO}_2$  storage projects such as the Frio project (observation well 30 m away) (Hovorka et al., 2006; Krevor et al., 2015) and the Sleipner project (observation 100 – 500 m away) (Chadwick et al., 2005). Whereas for the Otway (Observation well 170 m away) (Dance et al., 2019) and the Nagaoka project (Observation wells 40 m and 60 m away) (Mito and Xue, 2011; Sato et al., 2011), lower  $\text{CO}_2$  saturation values ( $\leq 0.6$ ) away from the injection well have been reported. Permeability and the degree of heterogeneity may have affected plume migration at different sites. Both the Frio (2 – 4 d) (Hovorka et al., 2006) and the Sleipner (>1 d) (Eiken et al., 2011) sites have high permeability values, whereas the Otway site has a large range of permeability values anywhere from 0.001 md to 10 d (Dance et al., 2019), and the Nagaoka site has rather low permeability values (0.5 – 12 md) (Sato et al., 2011). Because the permeability of the vertical slice domain we are working with in this study is relatively low, we would likely expect the post-drainage  $\text{CO}_2$  saturation to be low as well when measured away from the injection well.

After imbibition, the  $\text{CO}_2$  saturation map with capillary heterogeneity trapping is shown in Fig. 12E. 79% of the initial  $\text{CO}_2$  is trapped as residual  $\text{CO}_2$  saturation, comparing to 46% with pore-scale trapping only. Consequently, capillary heterogeneity trapping contributes 42% to the total  $\text{CO}_2$  volume that is residually trapped. By comparing the residual trapping results and capillary pressure curves with and without capillary heterogeneity trapping in Figs. 12 and 13, it is clear that with macroscopic trapping rules applied, many voxels with high initial  $\text{CO}_2$  saturation values now have high amounts of capillary heterogeneity trapping, which would have escaped otherwise.

#### 4. Conclusions

An MP simulator has been developed to simulate  $\text{CO}_2$ /water post-drainage and post-imbibition  $\text{CO}_2$  saturation distribution with capillary heterogeneity trapping under capillary and gravity dominated flow regimes. The MP simulator has been validated by a full-physics simulator, MRST, and can achieve a speedup of 10 to 100 times. An example of how the MP simulator can be applied to a field-scale vertical reservoir slice has also been shown. From the MP simulation results, the following conclusions can be drawn.

- There are significant differences observed between the voxel-level and the domain-level IR trapping relationships for heterogeneous

rocks, suggesting that approaches such as the one described here need to be taken in order to correctly compute the effective trapping characteristics of a heterogeneous domain.

- For uncorrelated random domains and for cases with downstream capillary barrier layers that are nonleaky, post-imbibition capillary heterogeneity trapping always increases with the degree of mesoscale heterogeneity, which is consistent with previous experimental results, although the relationship between  $A_d$  and  $std_{max}(S_{\text{CO}_2})$  is not linear as previously shown.
- Even when the degrees of mesoscale heterogeneity are the same, the spatial distribution of heterogeneity significantly affects the amount of capillary heterogeneity trapping achieved. Domains with nonleaky capillary barriers trap more than domains that are uncorrelated and random, which in turn trap more than domains with leaky barriers.
- The heterogeneity case with residual trapping abilities that best fit the experimental data suggests that domains with few capillary barriers and are otherwise homogenous can still achieve a significant amount of capillary heterogeneity trapping.

Overall, the simulation results presented in this study highlight the benefits of having a higher degree of heterogeneity and good capillary barriers at the mesoscale for increasing post-imbibition capillary heterogeneity trapping.

#### Declaration of Competing Interest

The authors declare that they have no known competing financial interests or personal relationships that could have appeared to influence the work reported in this paper.

#### CRediT authorship contribution statement

**Hailun Ni:** Methodology, Software, Visualization, Validation, Writing – original draft. **Olav Møyner:** Software, Writing – review & editing. **Kuncho D. Kurtev:** Resources. **Sally M. Benson:** Conceptualization, Supervision, Funding acquisition, Writing – review & editing.

#### Acknowledgement

This work was supported by Stanford University's Global Climate & Energy Project and the GeoQuest project funded by BHP. The GeoQuest project is a collaboration between the University of Melbourne, Cambridge University, and Stanford University. The authors thank the CO2CRC Ltd. for providing the geological data from the Otway International Test Centre supporting this study. The authors have no known financial conflicts of interests. All MP and MRST simulation codes can be found online at <http://dx.doi.org/10.17632/6gj3rd7ntr.2>.

## Supplementary materials

Supplementary material associated with this article can be found, in the online version, at doi:10.1016/j.advwatres.2021.103990.

### Appendix A. Sensitivity of the residual trapping simulation results

Both the pore-scale trapping ability  $A_p$  and the imbibition snap-off capillary pressure  $P_s$  have a large effect on the residual trapping amount simulated. In the MP simulation,  $A_p$  solely determines the amount of residual trapping that is caused by the pore-scale snap-off/bypass trapping mechanism at the voxel level, and  $P_s$  largely determines the amount of residual trapping that is caused by the mesoscale capillary heterogeneity trapping mechanism at the domain level. In order to explore the effect of  $A_p$  and  $P_s$  on residual trapping simulation results, a sensitivity analysis is provided here. The residual trapping results for the four synthetic cube domains are shown in Fig. A1. Sensitivity of the residual trapping simulation results to the tessellation pattern and the grid size is also discussed.

Fig. A1A shows that other than the leaky barrier case, all the other cases have their domain trapping ability  $A_d$  increase linearly with the  $P_s$  value. The rate of increase differs depending on the type of heterogeneity of the domain. We can see that having a nonzero  $P_s$  value is essential for capturing any capillary heterogeneity trapping. Because the leaky barrier case does not have a completely sealing capillary barrier, it has no extra amount of capillary heterogeneity trapping regardless of the value of  $P_s$  and regardless of the degree of heterogeneity of the domain, as we have previously discussed. Physically,  $P_s$  determines the voxel-level capillary pressure at which the pore-scale residual trapping amount is reached. The higher the  $P_s$  value, the sooner this particular voxel will reach its pore-scale residual trapping amount and get frozen during the imbibition MP simulation. With more voxels frozen early on during imbibition, the remaining voxels will have higher chances of been macroscopically trapped, and therefore the domain is likely to have a greater amount of capillary heterogeneity trapping as a result.

Fig. A1B shows that the  $A_d$  value for all types of domains increases linearly at different rates with the  $A_p$  value. The leaky barrier case has a unit slope, again indicating that no extra capillary heterogeneity trapping can be achieved above the  $A_p$  value. The results of this sensitivity study have demonstrated that for any given domain with a reasonable degree of heterogeneity, the  $A_d$  value changes linearly with  $P_s$  and  $A_p$ .

However, when a domain has an extremely high degree of heterogeneity, then the previous linear relationship between the input parameters  $P_s$ ,  $A_p$  and the output  $A_d$  value breaks down. This is because when the barriers in the domain have extremely low permeability, no matter how the value of  $P_s$  and  $A_p$  changes, during imbibition the water phase would not have enough driving forces to push the  $\text{CO}_2$  through the barrier and therefore the  $A_d$  value is always 1. For sensitivity analysis results on highly heterogeneous domains, see supplementary material.

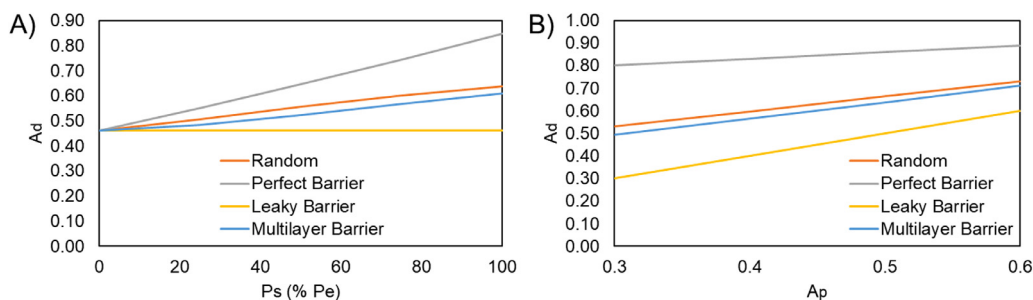


Fig. A1. Sensitivity of  $A_d$  to the  $P_s$  and the  $A_p$  values for the four different kinds of synthetic domains. The unit of  $P_s$  is the percentage of the capillary entry pressure  $P_e$  and ranges from 0 to 100% of the value of  $P_e$ .  $A_p = 0.46$  for all cases in A.  $P_s = P_e$  for all cases in B. The cases selected to represent the four domains are the MRST validation cases 3, 6, 7, and 8. Details about these cases can be found in Appendix B and the supplementary material.

In the presence of spatial correlations, the coordination number of the percolation lattice no longer affects the percolation threshold (Ioannidis et al., 1996). In the current study, all the synthetic barrier domains and the field-scale slice domains used have some kinds of spatial correlation present. The only domain without any spatial correlations is the random synthetic domain case. For this particular case, it is true that if other types of space-filling tessellation are chosen, the residual trapping simulation results may be different. This is because the different percolation threshold values will affect at what initial  $\text{CO}_2$  saturation the  $\text{CO}_2$  phase percolates the domain, which determines the point at which the domain-level IR plot starts deviating from the 100% trapping line. The coordination number also determines how easily a voxel can be macroscopically trapped. Generally a smaller coordination number promotes more macroscopic trapping. However, the general trapping trends observed here should still remain valid regardless of the tessellation chosen, that more heterogeneous domains will have more capillary heterogeneity (macroscopic) trapping.

To demonstrate the validity of the residual trapping results in Fig. 11 at larger domain sizes, extra MP simulation cases with the domain size  $100 \times 100 \times 100$  voxels have also been run for all the four major types of synthetic cube domains. For the random, perfect barrier, and the leaky barrier cases, the larger domain simulation results are highly similar to the results from the corresponding smaller domains. The differences in the domain average linear trapping coefficient  $A_d$  are all within 0.01. The only exception is the multilayer barrier case. Because the permeability value of its barrier voxels draws from a log-normal distribution, with just two layers of capillary barrier voxels and a much larger barrier size, there is a much higher chance that certain voxels on the barriers have similar permeability values as the upstream matrix. As a consequence, the multilayer barrier acts like a leaky barrier and no extra capillary heterogeneity trapping can be achieved in the larger domain. Therefore, for the larger domain size of the multilayer barrier case to achieve similar results as the smaller domain size, either more layers of capillary barriers need to be added, or the mean/standard deviation of the barrier permeability values need to be reduced.

### Appendix B. Validation of the MP simulator

In order to validate the MP simulation results, we compare with the results from a full-physics reservoir simulator, the MRST (Lie, 2019). The advantage of using MRST is that it is MATLAB-based so it is easy to use and to visualize simulation results. Also, as the source code is open, it allows fully customizable capillary pressure and relative permeability inputs for both drainage and imbibition. Furthermore, it is easy to turn gravity on or off. Because MRST is a full-physics simulator, some extra inputs are necessary to specify a flow scenario. Note that we use the two-phase black oil simulator module, treating  $\text{CO}_2$  as the oil phase and water as the water phase. The discretization used by the simulator is a fully-implicit scheme with two-point flux approximation and single-

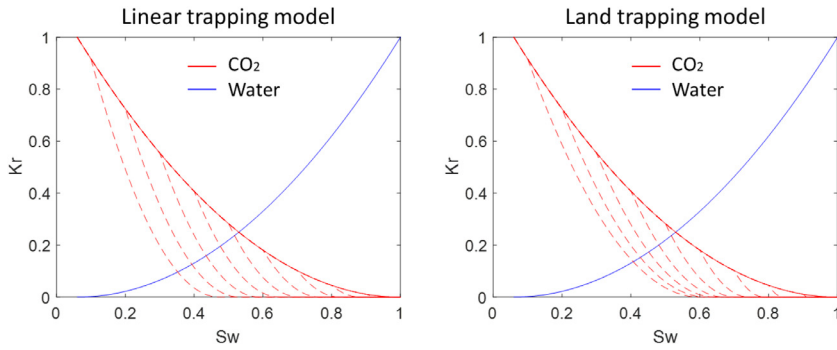


**Fig. B1.** Illustration of the voxel-level relative permeability model for both drainage and imbibition. Left: the linear trapping model. Right: the Land trapping model. Dashed lines are imbibition hysteresis scanning curves.

point mobility upwind, identical in configuration to most commercially available full-physics simulators.

**B.1 MRST validation inputs**

Ten simulation cases are run for validation. These cases have the same domain sizes as the previous trapping ability simulation cases. Among the ten validation cases, several different parameters are varied so that all simulation cases covered in the current study are validated. The validation cases include the following, homogeneous domains with different imbibition snap-off capillary pressure,  $P_s$  (cases 1 and 2); uncorrelated heterogeneous domains with an increasing degree of heterogeneity (cases 3 and 4); a heterogeneous domain with a different trapping model (case 5); heterogeneous domains with different types of downstream capillary barrier (cases 6,7, and 8); an uncorrelated heterogeneous slice domain (case 9); finally, a homogeneous domain with gravity forces added (case 10). Details of the input parameters for the ten validation cases are shown in supplementary material.

Capillary heterogeneity trapping is included for all validation cases in the MP simulator. In order to match MP simulation results to the full-physics simulation results, the maximum drainage capillary pressure for MP simulations is set to the median value of the resulting drainage capillary pressure field obtained from running the full-physics simulation. In order to minimize capillary end effects in MRST simulation, five slices are added both at the inlet and the outlet. The extra slices have uniform core average properties. A constant flux boundary condition is applied at the inlet and a constant pressure boundary condition of 1300 psia is applied at the outlet. All other boundaries are no-flow boundaries. CO<sub>2</sub> and water fluid properties are taken at 50 °C and 1300 psia. During drainage 100% CO<sub>2</sub> is injected. During imbibition 100% water is injected. A relatively high flow rate (5 mL/min) during drainage is used to establish enough capillary pressure in the domain, and a very low flow rate (0.01 mL/min) is used during imbibition to reach capillary dominated flow regimes. To ensure steady state is reached and to check for persistence of the trapped CO<sub>2</sub> saturation, both drainage and imbibition simulation are run for 50 PVI. For the single validation case involving gravity, the voxel sizes are increased to 2 dm × 2 dm × 2 dm so that obvious gravity effects are present. A low drainage flow rate (0.1 mL/min) is used for this case to ensure that the domain capillary-gravity equilibrium is established, and a higher imbibition flow rate (1 mL/min) is used to ensure full water sweep of the domain.

The most important additional simulation input that MRST requires but MP simulator does not is relative permeability. For MRST simulations, a single set of drainage relative permeability curves is used for the entire domain. For the imbibition relative permeability curves, we assume that no hysteresis exists in the water relative permeability curve for strongly water-wet sandstones (Ruprecht et al., 2014). Hysteresis is then only present in the CO<sub>2</sub> relative permeability curve. Either the linear or the Land trapping model can be used to determine the hysteretic CO<sub>2</sub> scanning curves. The equations for the voxel-level relative permeability model are shown in Eqs. (B1) to (B4) (Ruprecht et al., 2014),

$$k_{r,w}^{D, I} = S_w^{*N_w} \tag{B1}$$

**Table B1**

Values of the additional input parameters used in the fluid model in MRST simulation (Lemmon et al., 2018).

Parameter	Value
Water viscosity	0.54854 cp
CO <sub>2</sub> viscosity	0.023009 cp
Water density	991.86 kg/m <sup>3</sup>
CO <sub>2</sub> density	282.08 kg/m <sup>3</sup>
Water relative permeability coefficient $N_w$	2
CO <sub>2</sub> drainage relative permeability coefficient $N_{nw,D}$	2
CO <sub>2</sub> imbibition relative permeability coefficient $N_{nw,I}$	2

$$k_{r,nw}^D = (1 - S_w^*)^{N_{nw,D}} \tag{B2}$$

$$k_{r,nw}^I = (1 - \hat{S}_w^*)^{N_{nw,I}} \tag{B3}$$

$$\hat{S}_w^* = \frac{S_w - S_{wi}}{1 - S_{wi} - S_{nw,r}} \tag{B4}$$

where  $k_{r,w}$  is the wetting phase (water) relative permeability,  $k_{r,nw}$  is the nonwetting phase (CO<sub>2</sub>) relative permeability, superscript and subscript D represents drainage, and I represents imbibition. Eqs. (B1) to (B4) show the commonly used power model relative permeability for both drainage and imbibition. Eq. (B4) calculates the imbibition effective water saturation  $\hat{S}_w^*$ , where the  $S_{nw,r}$  value can be obtained either from the linear trapping relationship (Eq. (8)) or the Land trapping relationship (Eq. (12)). The illustration of the voxel-level relative permeability curves is shown in Fig. B1. Table B1 shows all the additional input parameter values used in the fluid model in MRST simulations. Note that when the flow rate is low and the flow regime is strongly capillary dominated, the exact shape of the relative permeability does not significantly impact the final equilibrium saturation field as long as the endpoints are the same. We have varied both the water and the CO<sub>2</sub> relative permeability coefficients from 2 to 5 during MRST imbibition simulations. The resulting MRST domain average residual CO<sub>2</sub> saturation values differ by 0.01 or less when compared to the corresponding MP values.

One last simulation decision that deserves extra attention is the choice of whether to have hysteresis in only the capillary pressure curves, only the relative permeability curves, or both. When hysteresis is present only in capillary pressure, because CO<sub>2</sub> is always mobile according to the relative permeability curves, eventually when steady state is reached during imbibition after many PVI, all CO<sub>2</sub> saturation goes to 0, with no residual trapping at all. When hysteresis is present only in relative permeability, because CO<sub>2</sub> remains mobile until each voxel reaches the residual saturation, saturation of the entire domain always goes down to exactly the voxel-level residual CO<sub>2</sub> saturation amount, with no extra capillary heterogeneity trapping. Hence, the desired case that most accurately represents the actual fluid physics in reality would

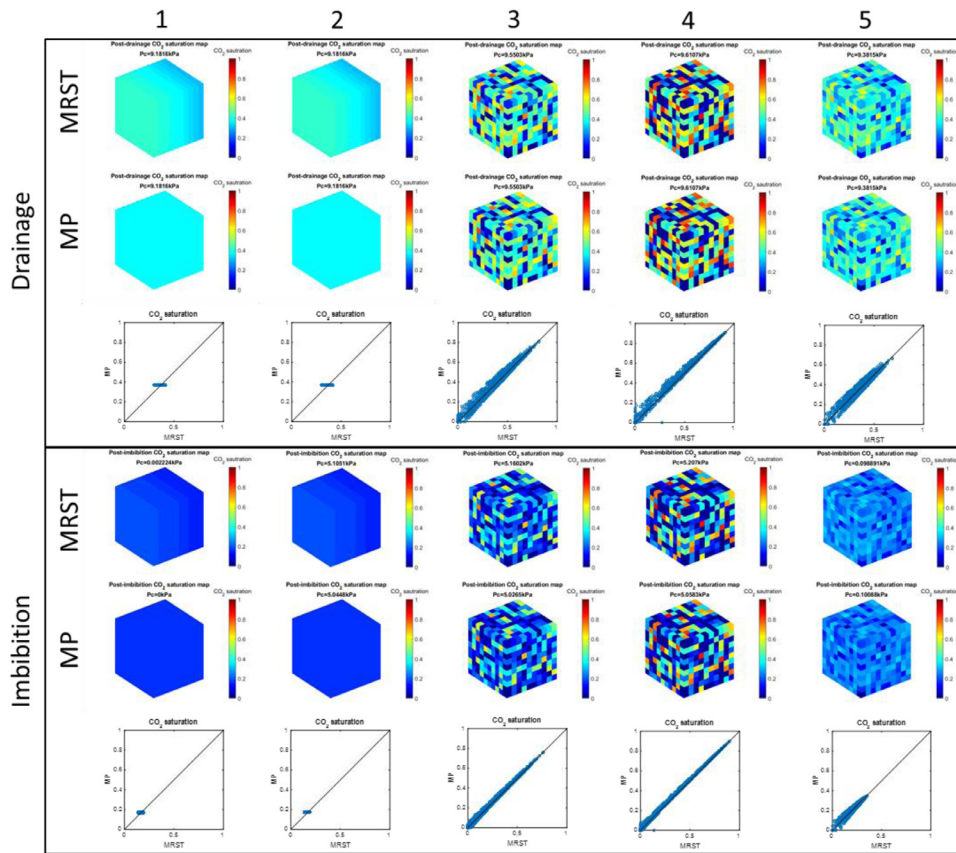


**Fig. B2.** Comparing MP and MRST simulation results for the first set of five validation cases. Row 1: MRST post-drainage CO<sub>2</sub> saturation maps. Row 2: MP post-drainage CO<sub>2</sub> saturation maps. Row 3: Scatter plots comparing goodness of match between the MP and MRST drainage results. Row 4 – 6: Same as Row 1 – 3 but for imbibition.

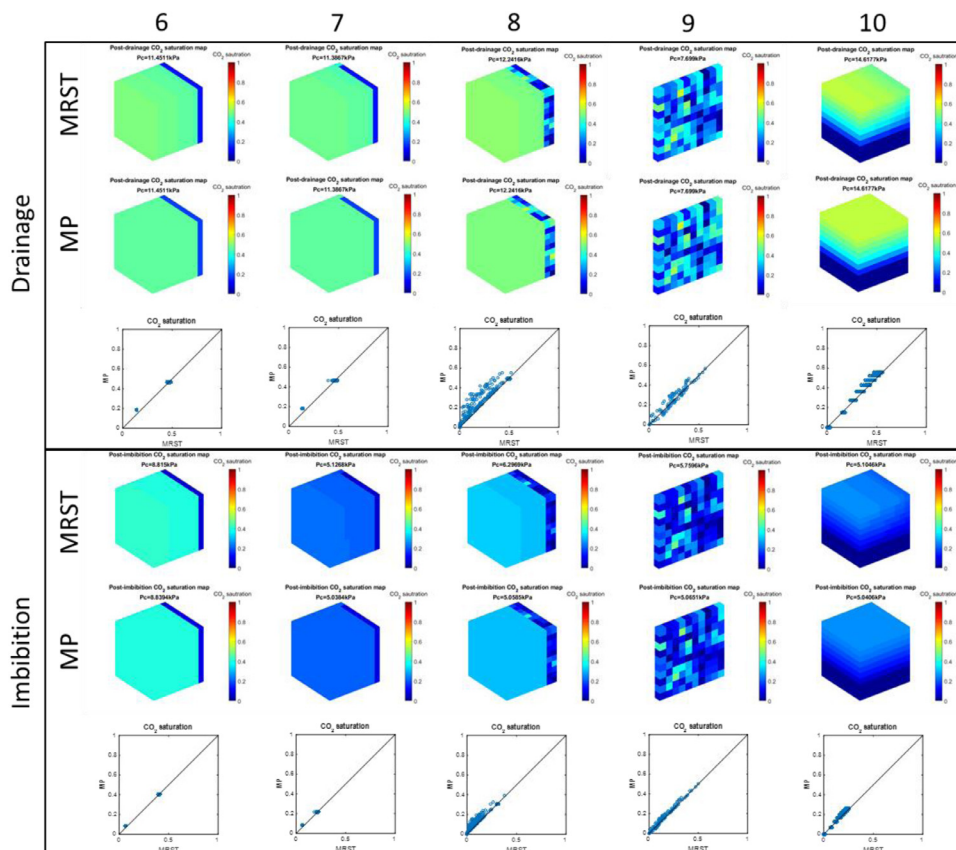


**Fig. B3.** Comparing MP and MRST simulation results for the second set of five validation cases. For detailed description, see Figure B2 caption.

be to have hysteresis present in both capillary pressure and relative permeability. And this is the case we run in MRST imbibition simulation to validate MP simulation results in this study.

### B.2 MRST validation results

Ten different validation cases are simulated and the MP simulation results are compared with the corresponding MRST simulation results here. All simulation results for the validation cases are shown in Figs. B2 and B3. The numerical values for the validation results can be found in supplementary material. In general, the MP simulation runs 10 to 100 times faster than the equivalent MRST simulation. MRST needs to take small time steps when the domain degree of heterogeneity is high or when the injection flow rate is low, and runs especially slowly under these circumstances as a result. Sometimes if the property field is extremely heterogeneous and discontinuous, when combined with a low flow rate, MRST's solver cannot converge no matter how much the time steps are cut.

From Fig. B2 and Fig. B3, it can be seen that the degree of match between the MP and the MRST simulation results is very good. The MP and MRST simulated saturation maps appear highly similar except the cases where capillary gradients can be seen particularly in the MRST post-drainage results such as cases 1 and 2. The mismatch in domain average CO<sub>2</sub> saturation is at 0.01 or less for all cases for both drainage and imbibition results. From the scatter plots of the voxel-level CO<sub>2</sub> saturation values in Figs. B2 and B3, we can see that cases 1 to 5 have almost perfect matches for both drainage and imbibition. For cases 6 to 10, while the vast majority of the voxels do match up well, the MP simulator tends to overestimate the CO<sub>2</sub> saturation at the end of drainage for a small portion of the voxels at the outlet because the MP simulator does not simulate the capillary end effects that are present in the MRST results during drainage. As a consequence of the good match in the CO<sub>2</sub> saturation fields, the estimated value for the domain effective linear trapping coefficient,  $A_d$ , from MP simulation is within 0.01 of the MRST values for all validation cases.

From the results for cases 1 and 2 in Fig. B2, we can see the effect of varying the value of  $P_s$  on homogeneous domains. Because there is no heterogeneity present in the domain, the overall post-imbibition CO<sub>2</sub> residual trapping amount remains the same with no extra capillary heterogeneity trapping achieved. However, as the degree of mesoscale heterogeneity increases, when  $P_s$  is nonzero, a significant amount of capillary heterogeneity trapping can be obtained, as can be seen by comparing the results for cases 2, 3, and 4.

## References

- Akin, S., Schembre, J.M., Bhat, S.K., Kovscek, a.R., 2000. Spontaneous imbibition characteristics of diatomite. *J. Pet. Sci. Eng.* 25, 149–165. [https://doi.org/10.1016/S0920-4105\(00\)00010-3](https://doi.org/10.1016/S0920-4105(00)00010-3).
- Al-Menhali, A.S., Krevor, S., 2016. Capillary trapping of CO<sub>2</sub> in oil reservoirs: observations in a mixed-wet carbonate rock. *Environ. Sci. Technol.* 50, 2727–2734. <https://doi.org/10.1021/acs.est.5b05925>.
- Bech, N., Frykman, P., 2018. Trapping of buoyancy-driven CO<sub>2</sub> during imbibition. *Int. J. Greenh. Gas Control* 78, 48–61. <https://doi.org/10.1016/j.ijggc.2018.06.018>.
- Behzadi, H., Alvarado, V., Mallick, S., 2011. CO<sub>2</sub> saturation, distribution and seismic response in two-dimensional permeability model. *Environ. Sci. Technol.* 45, 9435–9441. <https://doi.org/10.1021/es201969a>.
- Brooks, R.H., Corey, A.T., 1964. *Hydraulic properties of porous media*. *Color. State Univ. Hydrol. Pap.* 3, 1–27.
- Cavanagh, A.J., Haszeldine, R.S., 2014. The Sleipner storage site: capillary flow modeling of a layered CO<sub>2</sub> plume requires fractured shale barriers within the Utsira Formation. *Int. J. Greenh. Gas Control* 21, 101–112. <https://doi.org/10.1016/j.ijggc.2013.11.017>.
- Celia, M.A., Bachu, S., Nordbotten, J.M., Bandilla, K.W., 2015. Status of CO<sub>2</sub> storage in deep saline aquifers with emphasis on modeling approaches and practical simulations. *Water Resour. Res.* 51, 6846–6892. <https://doi.org/10.1002/2015WR017609>.
- Chadwick, R.A., Arts, R., EIKEN, O., 2005. 4D seismic quantification of a growing CO<sub>2</sub> plume at Sleipner, North Sea. In: Dore, A.G., Vining, B.A. (Eds.), *Petroleum Geology: North-West Europe and Global Perspectives—Proceedings of the 6th Petroleum Geology Conference*. the Geological Society, London, pp. 1385–1399.
- Cinar, Y., Riaz, A., Tchepeli, H.A., 2007. Experimental study of CO<sub>2</sub> injection into saline formations. *SPE Annu. Tech. Conf. Proc.* 5, 3363–3372. <https://doi.org/10.2523/110628-ms>.
- Corbett, P.W.M., Ringrose, P.S., Jensen, J.L., Sorbie, K.S., 1992. Laminated clastic reservoirs: the interplay of capillary pressure and sedimentary architecture. In: *SPE Annual Technical Conference and Exhibition*. Society of Petroleum Engineers, pp. 365–376. <https://doi.org/10.2118/24699-MS>.
- Dance, T., LaForce, T., Glubokovskikh, S., Ennis-King, J., Pevzner, R., 2019. Illuminating the geology: post-injection reservoir characterisation of the CO<sub>2</sub> CRC Otway site. *Int. J. Greenh. Gas Control* 86, 146–157. <https://doi.org/10.1016/j.ijggc.2019.05.004>.
- Eiken, O., Ringrose, P., Hermanrud, C., Nazarian, B., Torp, T.A., Høier, L., 2011. Lessons learned from 14 years of CCS operations: sleipner, in Salah and Snøhvit. *Energy Procedia* 4, 5541–5548. <https://doi.org/10.1016/j.egypro.2011.02.541>.
- Engelberts, W.F., Klinkenberg, L.J., 1951. Laboratory experiments on the displacement of oil by water from packs of granular material. In: *3rd World Petroleum Congress*. World Petroleum Congress, pp. 544–554.
- Gershenson, N.I., Ritz, R.W., Dominic, D.F., Mehnert, E., Okwen, R.T., 2017. Capillary trapping of CO<sub>2</sub> in heterogeneous reservoirs during the injection period. *Int. J. Greenh. Gas Control* 59, 13–23. <https://doi.org/10.1016/j.ijggc.2017.02.002>.
- Hovorka, S.D., Benson, S.M., Doughty, C., Freifeld, B.M., Sakurai, S., Daley, T.M., Kharaka, Y.K., Holtz, M.H., Trautz, R.C., Nance, H.S., Myer, L.R., Knauss, K.G., 2006. Measuring permanence of CO<sub>2</sub> storage in saline formations: the Frio experiment. *Environ. Geosci.* 13, 105–121. <https://doi.org/10.1306/eg.11210505011>.
- Huang, Y., Ringrose, P.S., Sorbie, K.S., 1995. Capillary trapping mechanisms in water-wet laminated rocks. *SPE Reserv. Eng.* 10, 287–292. <https://doi.org/10.2118/28942-PA>.
- Ioannidis, M.A., Chatzis, I., Dullien, F.A.L., 1996. Macroscopic percolation model of immiscible displacement: effects of buoyancy and spatial structure. *Water Resour. Res.* 32, 3297–3310. <https://doi.org/10.1029/95WR02216>.
- IPCC, 2014. *Climate Change 2014: Mitigation of Climate Change. Contribution of Working Group III to the Fifth Assessment Report of the Intergovernmental Panel on Climate Change*. Cambridge University Press, Cambridge, United Kingdom and New York, NY, USA.
- IPCC, 2005. *IPCC Special Report on Carbon Dioxide Capture and Storage*. Prepared by Working Group III of the Intergovernmental Panel on Climate Change, IPCC Special Report on Carbon Dioxide Capture and Storage. Cambridge University Press, Cambridge, United Kingdom and New York, NY, USA.
- Jackson, S.J., Krevor, S., 2020. Small-scale capillary heterogeneity linked to rapid plume migration during CO<sub>2</sub> storage. *Geophys. Res. Lett.* 47. <https://doi.org/10.1029/2020GL088616>.
- Jackson, S.J., Krevor, S., 2019. Characterization of hysteretic multiphase flow from the MM to M scale in heterogeneous rocks. *E3S Web Conf.* 89, 02001. <https://doi.org/10.1051/e3sconf/20198902001>.
- Jackson, S.J., Lin, Q., Krevor, S., 2020. Representative elementary volumes, hysteresis, and heterogeneity in multiphase flow from the pore to continuum scale. *Water Resour. Res.* 56, 1–33. <https://doi.org/10.1029/2019WR026396>.
- Kimbrel, E.H., Herring, A.L., Armstrong, R.T., Lunati, I., Bay, B.K., Wildenschild, D., 2015. Experimental characterization of nonwetting phase trapping and implications for geologic CO<sub>2</sub> sequestration. *Int. J. Greenh. Gas Control* 42, 1–15. <https://doi.org/10.1016/j.ijggc.2015.07.011>.
- Kortekaas, T., 1985. Water/Oil displacement characteristics in crossbedded reservoir zones. *Soc. Pet. Eng. J.* 25, 917–926. <https://doi.org/10.2118/12112-PA>.
- Krause, M., Krevor, S., Benson, S.M., 2013. A Procedure for the accurate determination of sub-core scale permeability distributions with error quantification. *Transp. Porous Media* 98, 565–588. <https://doi.org/10.1007/s11242-013-0161-y>.
- Krause, M., Perrin, J., Benson, S.M., 2011. Modeling permeability distributions in a sandstone core for history matching coreflood experiments. In: *2009 SPE International Conference on CO<sub>2</sub> Capture, Storage and Utilization*, pp. 768–777. <https://doi.org/10.2118/126340-MS>.
- Krevor, S., Blunt, M.J., Benson, S.M., Pentland, C.H., Reynolds, C., Al-Menhali, A., Niu, B., 2015. Capillary trapping for geologic carbon dioxide storage – from pore scale physics to field scale implications. *Int. J. Greenh. Gas Control* 40, 221–237. <https://doi.org/10.1016/j.ijggc.2015.04.006>.
- Krevor, S.C.M., Pini, R., Li, B., Benson, S.M., 2011. Capillary heterogeneity trapping of CO<sub>2</sub> in a sandstone rock at reservoir conditions. *Geophys. Res. Lett.* 38. <https://doi.org/10.1029/2011GL048239>.
- Krevor, S.C.M., Pini, R., Zuo, L., Benson, S.M., 2012. Relative permeability and trapping of CO<sub>2</sub> and water in sandstone rocks at reservoir conditions. *Water Resour. Res.* 48. <https://doi.org/10.1029/2011WR010859>.
- Kueper, B.H., McWhorter, D.B., 1992. The use of macroscopic percolation theory to construct large-scale capillary pressure curves. *Water Resour. Res.* 28, 2425–2436. <https://doi.org/10.1029/92wr01176>.
- Kuo, C.-W., Benson, S.M., 2015. Numerical and analytical study of effects of small scale heterogeneity on CO<sub>2</sub>/brine multiphase flow system in horizontal corefloods. *Adv. Water Resour.* 79, 1–17. <https://doi.org/10.1016/j.advwatres.2015.01.012>.
- Land, C., 1968. Calculation of imbibition relative permeability for two- and three-phase flow from rock properties. *SPE J.* 8, 149–156. <https://doi.org/10.2118/1942-PA>.
- Larkin, R.G., 2010. Hydrodynamic trapping of CO<sub>2</sub> geosequestered in saline aquifers. *SPE Improved Oil Recovery Symposium*. Society of Petroleum Engineers, Tulsa, Oklahoma. <https://doi.org/10.2118/128205-MS>.
- Lefebvre du Prey, E.J., 1973. Factors affecting liquid-liquid relative permeabilities of a consolidated porous medium. *Soc. Pet. Eng. J.* 13, 39–47. <https://doi.org/10.2118/3039-PA>.
- Lemmon, E.W., McLinden, M.O., Friend, D.G., 2018. Thermophysical properties of fluid systems [WWW Document]. NIST Chem. WebBook, NIST Stand. Ref. Database Number 69. <https://doi.org/10.18434/T4D303>.
- Leverett, M.C., 1941. Capillary behavior in porous solids. *Trans. AIME* 142, 152–169. <https://doi.org/10.2118/941152-G>.
- Li, B., Benson, S.M., 2015. Influence of small-scale heterogeneity on upward CO<sub>2</sub> plume migration in storage aquifers. *Adv. Water Resour.* 83, 389–404. <https://doi.org/10.1016/j.advwatres.2015.07.010>.

- Lie, K.-A., 2019. An Introduction to Reservoir Simulation Using MATLAB/GNU Octave: User Guide For the MATLAB Reservoir Simulation Toolbox (MRST). Cambridge University Press. <https://doi.org/10.1017/9781108591416>.
- Meckel, T.A., Bryant, S.L., 2014. Buoyancy-driven flow in heterogeneous materials. *Energy Procedia* 63, 5495–5502. <https://doi.org/10.1016/j.egypro.2014.11.582>.
- Meckel, T.A., Bryant, S.L., Ravi Ganesh, P., 2015. Characterization and prediction of CO<sub>2</sub> saturation resulting from modeling buoyant fluid migration in 2D heterogeneous geologic fabrics. *Int. J. Greenh. Gas Control* 34, 85–96. <https://doi.org/10.1016/j.ijggc.2014.12.010>.
- Mishra, A., Kurtev, K.D., Haese, R.R., 2020. Composite rock types as part of a workflow for the integration of mm-to cm-scale lithological heterogeneity in static reservoir models. *Mar. Pet. Geol.* 114, 104240. <https://doi.org/10.1016/j.marpetgeo.2020.104240>.
- Mishra, A., Pajank, L., Haese, R.R., 2019. High resolution characterization of lithological heterogeneity of the paaratte formation, otway basin (australia), a coastal to shallow-marine deposit. *Geosci* 9. <https://doi.org/10.3390/geosciences9060278>.
- Mito, S., Xue, Z., 2011. Post-injection monitoring of stored CO<sub>2</sub> at the Nagaoka Pilot Site : 5 years time-lapse well logging results. *Energy Procedia* 4, 3284–3289. <https://doi.org/10.1016/j.egypro.2011.02.248>.
- Morrow, N.R., Chatzis, I., Taber, J.J., 1988. Entrapment and mobilization of residual oil in bead packs. *SPE Reserv. Eng.* 3, 927–934. <https://doi.org/10.2118/14423-PA>.
- Ni, H., Boon, M., Garing, C., Benson, S.M., 2019. Predicting CO<sub>2</sub> residual trapping ability based on experimental petrophysical properties for different sandstone types. *Int. J. Greenh. Gas Control* 86, 158–176. <https://doi.org/10.1016/j.ijggc.2019.04.024>.
- Niu, B., Al-Menhali, A., Krevor, S.C., 2015. The impact of reservoir conditions on the residual trapping of carbon dioxide in Berea sandstone. *Water Resour. Res.* 51, 2009–2029. <https://doi.org/10.1002/2014WR016441>.
- Nooruddin, H.A., Blunt, M.J., 2018. Large-scale invasion percolation with trapping for upscaling capillary-controlled darcy-scale flow. *Transp. Porous Media* 121, 479–506. <https://doi.org/10.1007/s11242-017-0960-7>.
- Pevzner, R., Urosevic, M., Caspari, E., Galvin, R.J., Madadi, M., Dance, T., Shulakova, V., Gurevich, B., Tcheverda, V., Cinar, Y., 2013. Feasibility of time-lapse seismic methodology for monitoring the injection of small quantities of CO<sub>2</sub> into a saline formation, CO<sub>2</sub>CRC otway project. *Energy Procedia* 37, 4336–4343. <https://doi.org/10.1016/j.egypro.2013.06.336>.
- Pini, R., Benson, S.M., 2017. Capillary pressure heterogeneity and hysteresis for the supercritical CO<sub>2</sub>/water system in a sandstone. *Adv. Water Resour.* 108, 277–292. <https://doi.org/10.1016/j.advwatres.2017.08.011>.
- Pini, R., Krevor, S., 2019. Chapter 7 - Laboratory Studies to Understand the Controls on Flow and Transport for CO<sub>2</sub> Storage, *Science of Carbon Storage in Deep Saline Formations*. Elsevier Inc <https://doi.org/https://doi.org/10.1016/B978-0-12-812752-0.00007-1>.
- Pini, R., Madonna, C., 2016. Moving across scales: a quantitative assessment of X-ray CT to measure the porosity of rocks. *J. Porous Mater.* 23, 325–338. <https://doi.org/10.1007/s10934-015-0085-8>.
- Ren, B., 2018. Local capillary trapping in carbon sequestration: parametric study and implications for leakage assessment. *Int. J. Greenh. Gas Control* 78, 135–147. <https://doi.org/10.1016/j.ijggc.2018.08.001>.
- Ren, B., Bryant, S.L., Lake, L.W., 2019. Estimating local capillary trap volume capacities using a geologic criterion. *Int. J. Greenh. Gas Control* 85, 46–57. <https://doi.org/10.1016/j.ijggc.2019.03.025>.
- Ren, B., Duncan, I., 2019. Modeling oil saturation evolution in residual oil zones: implications for CO<sub>2</sub> EOR and sequestration. *J. Pet. Sci. Eng.* <https://doi.org/10.1016/j.petrol.2019.02.072>.
- Reynolds, C.A., Blunt, M.J., Krevor, S., 2018. Multiphase flow characteristics of heterogeneous rocks from CO<sub>2</sub> storage reservoirs in the United Kingdom. *Water Resour. Res.* 729–745. <https://doi.org/10.1002/2017WR021651>.
- Rogelj, J., Shindell, D., Jiang, K., Fifita, S., Forster, P., Ginzburg, V., Handa, C., Kheshgi, H., Kobayashi, S., Kriegler, E., Mundaca, L., Séférian, R., Vilariño, M.V., 2018. Mitigation pathways compatible with 1.5°C in the context of sustainable development. In: Masson-Delmotte, V., Zhai, P., Pörtner, H.-O., Roberts, D., Skea, J., Shukla, P.R., Pirani, A., Moufouma-Okia, W., Péan, C., Pidcock, R., Connors, S., Matthews, J.B.R., Chen, Y., Zhou, X., Gomis, M.I., Lonnoy, E., Maycock, T., Tignor, M., Waterfield, T. (Eds.), *Global Warming of 1.5°C. An IPCC Special Report On the Impacts of Global Warming of 1.5°C Above Pre-Industrial Levels and Related Global Greenhouse Gas Emission Pathways, in the Context of Strengthening the Global Response to the Threat of Climate Change*, pp. 93–174.
- Ruprecht, C., Pini, R., Falta, R., Benson, S., Murdoch, L., 2014. Hysteretic trapping and relative permeability of CO<sub>2</sub> in sandstone at reservoir conditions. *Int. J. Greenh. Gas Control* 27, 15–27. <https://doi.org/10.1016/j.ijggc.2014.05.003>.
- Saadatpoor, E., Bryant, S.L., Sepehrmoori, K., 2013. Estimation of local capillary trapping capacity from geologic models. *Energy Procedia* 37, 5501–5510. <https://doi.org/10.1016/j.egypro.2013.06.470>.
- Saadatpoor, E., Bryant, S.L., Sepehrmoori, K., 2010. New trapping mechanism in carbon sequestration. *Transp. Porous Media* 82, 3–17. <https://doi.org/10.1007/s11242-009-9446-6>.
- Sato, K., Mito, S., Horie, T., Ohkuma, H., Saito, H., Watanabe, J., Yoshimura, T., 2011. Monitoring and simulation studies for assessing macro- and meso-scale migration of CO<sub>2</sub> sequestered in an onshore aquifer: experiences from the Nagaoka pilot site. *Japan. Int. J. Greenh. Gas Control* 5, 125–137. <https://doi.org/10.1016/j.ijggc.2010.03.003>.
- Tanino, Y., Blunt, M.J., 2013. Laboratory investigation of capillary trapping under mixed-wet conditions. *Water Resour. Res.* 49, 4311–4319. <https://doi.org/10.1002/wrcr.20344>.
- Trevisan, L., Krishnamurthy, P.G., Meckel, T.A., 2017a. Impact of 3D capillary heterogeneity and bedform architecture at the sub-meter scale on CO<sub>2</sub> saturation for buoyant flow in clastic aquifers. *Int. J. Greenh. Gas Control* 56, 237–249. <https://doi.org/10.1016/j.ijggc.2016.12.001>.
- Trevisan, Luca, Pini, R., Cihan, A., Birkholzer, J.T., Zhou, Q., González-Nicolás, A., Il-langasekare, T.H., 2017b. Imaging and quantification of spreading and trapping of carbon dioxide in saline aquifers using meter-scale laboratory experiments. *Water Resour. Res.* 53, 485–502. <https://doi.org/10.1002/2016WR019749>.
- Wilkinson, D., Willemsen, J.F., 1983. Invasion percolation: a new form of percolation theory. *J. Phys. A. Math. Gen.* 16, 3365–3376. <https://doi.org/10.1088/0305-4470/16/14/028>.
- Wolff, M., Flemisch, B., Helmig, R., 2013. An adaptive multiscale approach for modeling two-phase flow in porous media including capillary pressure. *Water Resour. Res.* 49, 8139–8159. <https://doi.org/10.1002/2013WR013800>.
- Yang, Z., Chen, Y.-F., Niemi, A., 2020. Gas migration and residual trapping in bimodal heterogeneous media during geological storage of CO<sub>2</sub>. *Adv. Water Resour.* 142, 103608. <https://doi.org/10.1016/J.ADVWATRES.2020.103608>.
- Yang, Z., Tian, L., Niemi, A., Fagerlund, F., 2013. Upscaling of the constitutive relationships for CO<sub>2</sub> migration in multimodal heterogeneous formations. *Int. J. Greenh. Gas Control* 19, 743–755. <https://doi.org/10.1016/j.ijggc.2012.11.015>.
- Yortsos, Y.C., Satik, C., Bacri, J.C., Salin, D., 1993. Large-scale percolation theory of drainage. *Transp. Porous Media* 10, 171–195. <https://doi.org/10.1007/BF00617007>.
- Zeybek, M., Gurakin, G., Donmez, A., Onur, M., 1995. Effects of Capillary Heterogeneities on Spontaneous Imbibition. *SPE*. <https://doi.org/10.2118/30778-MS>.